THESIS

MODELING THE FORMATION AND COMPOSITION OF SECONDARY ORGANIC AEROSOL FROM DIESEL EXHAUST USING PARAMETERIZED AND SEMI-EXPLICIT CHEMISTRY AND THERMODYNAMIC MODELS

Submitted by

Sailaja Eluri

Department of Mechanical Engineering

In partial fulfillment of the requirements

For the Degree of Master of Science

Colorado State University

Fort Collins, Colorado

Spring 2017

Master's Committee:

Advisor: Shantanu Jathar

John Volckens
Jeffrey Pierce
Delphine Farmer

ABSTRACT

MODELING THE FORMATION AND COMPOSITION OF SECONDARY ORGANIC AEROSOL FROM DIESEL EXHAUST USING PARAMETERIZED AND SEMI-EXPLICIT CHEMISTRY AND THERMODYNAMIC MODELS

Laboratory-based studies have shown that diesel-powered sources emit volatile organic compounds that can be photo-oxidized in the atmosphere to form secondary organic aerosol (SOA); in some cases, this SOA can exceed direct emissions of particulate matter (PM); PM is a criteria pollutant that is known to have adverse effects on air quality, climate, and human health. However, there are open questions surrounding how these laboratory experiments can be extrapolated to the real atmosphere and how they will help identify the most important species in diesel exhaust that contribute to SOA formation. Jathar et al. (2017) recently performed experiments using an oxidation flow reactor (OFR) to measure the photochemical production of SOA from a diesel engine operated at two different engine loads (idle, load), two fuel types (diesel, biodiesel) and two aftertreatment configurations (with and without an oxidation catalyst and particle filter). In this work, we will use two different SOA models, namely the volatility basis set (VBS) model and the statistical oxidation model (SOM), to simulate the formation, evolution and composition of SOA from the experiments of Jathar et al. (2017). Leveraging recent laboratory-based parameterizations, both frameworks accounted for a semi-volatile and reactive POA, SOA production from semi-volatile, intermediate-volatility and volatile organic compounds (SVOC, IVOC and VOC), NO_x-dependent multigenerational gas-phase chemistry,

and kinetic gas/particle partitioning. Both frameworks demonstrated that for model predictions of SOA mass and elemental composition to agree with measurements across all engine load-fuel-aftertreatment combinations, it was necessary to (a) model the kinetically-limited gas/particle partitioning likely in OFRs and (b) account for SOA formation from IVOCs (IVOCs were found to account for more than four-fifths of the model-predicted SOA). Model predictions of the gas-phase organic compounds (resolved in carbon and oxygen space) from the SOM compared favorably to gas-phase measurements made using a Chemical Ionization Mass Spectrometer (CIMS) that, qualitatively, substantiated the semi-explicit chemistry captured by the SOM and the measurements made by the CIMS. Sensitivity simulations suggested that (a) IVOCs from diesel exhaust could be modeled using a single surrogate species with an SOA mass yield equivalent to a C_{15} or C_{17} linear alkane for use in large-scale models, (b) different diesel exhaust emissions profiles in the literature resulted in the same SOA production as long as IVOCs were included and (c) accounting for vapor wall loss parameterizations for the SOA precursors improved model performance. As OFRs are increasingly used to study SOA formation and evolution in laboratory and field environments, there is a need to develop models that can be used to interpret the OFR data. This work is one example of the model development and application relevant to the use of OFRs.

ACKNOWLEDGEMENTS

First and foremost, I would like to thank my advisor, Dr. Shantanu Jathar, for his support and guidance in carrying out my research and providing the resources without which this work would not have been possible. He has been of enormous help in every possible way right from the time I joined his research group.

I would like to thank my graduate committee for their valuable time and effort in providing suggestions for the work.

I would also like to thank Dr. Beth Friedman and her advisor Dr. Delphine Farmer for providing measurement data and Dr. Christopher Cappa for sharing the Igor version of the Statistical Oxidation Model.

PREFACE

Fine particles or aerosols have been recognized for their negative impact on air quality, climate, and human health. Secondary organic particulate matter, or secondary organic aerosol (SOA), account for a significant fraction of ambient fine particulate matter yet there are large uncertainties surrounding the formation and evolution of SOA, which eventually determines their atmospheric burden and environmental impact. This work uses numerical models to study the formation, composition, and properties of SOA arising from diesel engines.

TABLE OF CONTENTS

LIST OF TABLES

LIST OF FIGURES

LIST OF SYMBOLS/ACRONYMS

POA – Primary Organic Aerosol

SOA- Secondary Organic Aerosol

THC - Total Hydrocarbons

OFR – Oxidation Flow Reactor

VOC -Volatile Organic Compounds

IVOC – Intermediate Volatile Organic Compounds

VBS - Volatility Basis Set

SOM – Statistical Oxidation Model

OA – Organic Aerosol

DPF – Diesel Particulate Filter

DOC – Diesel Oxidation Catalyst

GC-MS – Gas Chromatography Mass Spectrometer

HR-AMS- High Resolution Aerosol - Mass Spectrometer

CIMS – Chemical Ionization Mass Spectrometer

MW- Molecular Weight

C^*- Effective Saturation Concentration

OH – Hydroxyl Radical

NO_x – Nitrogen Oxides

CO_2 – Carbon di-oxide

CO – Carbon monoxide

O_2-Oxygen

O:C – Oxygen to Carbon ratio

α – Accommodation Coefficient

INTRODUCTION

Combustion sources such as motor vehicles, wood stoves, and wildfires emit fine-mode aerosols as products of incomplete combustion. Combustion-related aerosols are an important contributor to urban and global air pollution and have strong implications for climate (Pachauri et al., 2014), the environment (Jacobson et al.,2000), and human health (Anderson et al., 2012). While direct emissions from combustion sources are dominated by primary organic aerosol (POA) and black carbon (Bond et al., 2013), these sources also emit volatile organic compounds that can photochemically react in the atmosphere to form secondary organic aerosol (SOA) (Robinson et al., 2007). SOA, like POA, is a complex mixture of thousands of compounds with very different physical and chemical properties, some that vary over logarithmic scales (Goldstein and Galbally, 2007). Laboratory experiments have shown that when photochemically processed for a few hours, combustion emissions can produce enough SOA to exceed primary aerosol emissions (Jathar et al., 2014). However, this SOA production and the concurrent evolution of POA from combustion emissions is not very well represented in models in terms of its sources, gas/particle partitioning, composition and properties (Fuzzi et al., 2015). Further, three-dimensional air quality models frequently under-predict SOA mass concentrations during strong photochemical episodes in urban areas (Carlton et al., 2010), which likely highlights the deficiency in modeling the SOA contributions from urban, combustion-related emissions.

Robinson et al. (2007) performed one of the first environmental chamber experiments to measure photochemical production of SOA from diesel exhaust. They found that within a few hours of photochemical processing, SOA production doubled the primary aerosol mass. Although novel,

the diesel exhaust source used by Robinson et al. (2007) (small non-road diesel generator) was unrepresentative of sources found in the real world. Chirico et al. (2010) and Gordon et al. (2014) performed similar chamber experiments to measure photochemical production of SOA from diesel exhaust, although these were performed on tailpipe emissions from in-fleet, on-road diesel vehicles run on chassis dynamometers. Both found that their SOA production was roughly consistent with the findings from Robinson et al. (2007) but they also developed additional insights. They found that the use of aftertreatment devices (diesel oxidation catalysts and diesel particulate filters) substantially reduced SOA production (mimicking the reduction in primary aerosol emissions), but both also observed some SOA production during cold starts and/or regeneration events when the aftertreatment devices' functioning was limited. Gordon et al. (2014) also found negligible differences in the SOA formation between diesel and biodiesel fuel. To simulate longer timescales, Tkacik et al. (2014) measured SOA formation using an oxidation flow reactor (OFR) from air sampled from a highway tunnel in Pittsburgh, PA used by both on-road gasoline and diesel vehicles. Tkacik et al. (2014) measured much stronger SOA formation (SOA: POA was 10:1) over photochemical exposures equivalent to 2 to 3 days, but found that the SOA was lost or destroyed as the mixture continued to age over the timescale of a week. Recently, Jathar et al. (2017) performed experiments using an OFR similar to Tkacik et al. (2014) to measure the photochemical production of SOA from a diesel engine operated at various engine load-fuel-aftertreatment configurations. Efficient combustion at higher engine loads coupled to the removal of SOA precursors by aftertreatment systems reduced SOA production by factors of 2-10. The only exception was that the aftertreatment system did not reduce SOA production at idle loads possibly because the exhaust temperatures were low enough to limit removal of SOA precursors in the oxidation catalyst. In summary, it is clear that diesel

exhaust contributes to atmospheric SOA production although the precise production of SOA varies across dimensions of photochemical age, engine duty cycle, use of alternative fuels, and aftertreatment devices.

Most OFRs used to study SOA production have been 10-15 L, flow-through metal reactors with lamps that can produce high concentrations of atmospheric oxidants to simulate photochemical processing (e.g., Lambe et al., 2011). Flows through an OFR allow for residence times between one to three minutes but given the high oxidant concentrations, OFRs can simulate up to two weeks of photochemistry (Palm et al.,2016). OFRs have three distinct advantages over environmental chambers. First, OFRs are smaller in size and easier to operate than environmental chambers, which allows for shorter experiments and makes them ideal for field deployments (Palm et al., 2016). Second, production of high oxidant concentrations in OFRs allows for much longer photochemical exposures (~factor of 10) than those possible with chambers (Lambe et al., 2012). Third, OFRs have much smaller surface area-to-volume ratios when compared to conventional chambers (factor of ~10 lower) and hence are less susceptible to gas and particle losses (less than 10%(Palm et al., 2015) that are known to strongly influence SOA formation (Zhang et al., 2014; Krechmer et al., 2015). These advantages can be linked to the increasing use of OFRs in both laboratory and field experiments to study the formation and transformation of SOA (Ortega et al., 2016, Bruns et al., 2016, Palm et al., 2016). Despite these advantages, researchers are concerned that the accelerated chemistry (Palm et al., 2016) and limitations to gas/particle partitioning (Palm et al., 2016; Jathar et al., 2017) may affect the formation and composition of SOA in OFRs and question their relevance in understanding SOA formation in the real atmosphere. For instance, high oxidant concentrations in OFRs can enhance

fragmentation (or scission) of carbon-carbon bonds and lead to formation of higher volatility products (Kroll et al., 2009) that would consequently underpredict SOA production. In addition, the short residence times in OFRs and/or the small condensation sinks from preexisting aerosol may not allow for complete condensation of the SOA and also underpredict SOA formation. With the increased use of OFRs, there appears to be a need to develop modeling tools that for instance, can account for fragmentation reactions and kinetic gas/particle partitioning and allow us to accurately interpret the OFR data and make projections for the real atmosphere.

Models used to simulate the photochemical production of SOA from VOCs in combustion emissions have traditionally used the two-product (Odum et al., 1996) or the more generalized n-product volatility basis set (VBS) framework (Donahue et al., 2006). In this framework, VOC oxidation products are lumped into volatility bins based on their effective saturation concentrations (C*; saturation vapor pressure converted into mass concentration units) where the saturation concentration determines the partitioning of the products between the gas and particle phases (Pankow et al., 1994). Each VOC that forms SOA produces a unique product distribution in volatility space and these product distributions that essentially represent stable first-generation products have been determined for more than two dozen compounds using chamber experiments (e.g., Ng et al., 2007; Chhabra et al., 2010). The VBS framework has been widely used in both box (Dzepina et al., 2009; Hodzic et al., Jathar et al., 2014) and three-dimensional (Murphy and Pandis, 2009; Tsimpidi et al., 2010; Jathar et al., 2011; Ahmadov et al., 2014; Konovalov et al., 2015) models to simulate the chemistry and gas/particle partitioning of OA. In box models SOA production from each precursor can be tracked separately but in three-dimensional models where computational costs need to be considered, precursors that are similar in their potential to form

SOA are frequently lumped together. While the VBS approach offers an elegant and computationally efficient framework to model SOA formation, the VBS through a representation of volatility only neither tracks the molecular composition nor informs the continued multi-generational chemistry that will determine the atmospheric evolution and properties of SOA. For instance, VBS-type models have not been able to leverage observations of the elemental composition of SOA (e.g., atomic O:C ratios) that have become possible through the use of the aerosol mass spectrometer (AMS) to constrain VBS parameterizations or test VBS predictions. Further, most VBS-type models have employed ad hoc parameterizations to model multi-generational chemistry that do not account for fragmentation reactions (Robinson et al., 2007) and possibly double count SOA formation (Jathar et al., 2016). Therefore, there is a demand to develop models that can provide an improved representation of the chemistry that governs the formation, composition and properties of SOA.

Previously, VBS models have been used to predict photochemical production of SOA from diesel exhaust (Robinson et al., Jathar et al., 2014; Tkacik et al., 2014). These modeling studies have shown that traditionally speciated SOA precursors such as long alkanes ($C_{6\text{-}12}$) and single-ring aromatics (e.g., benzene, toluene) explain less than 20% of the observed SOA and have argued that the remainder of the SOA (more than 80%) arises from the photooxidation of typically unspeciated organic compounds. These unspeciated compounds, also referred to as intermediate volatility organic compounds (IVOCs), are likely species with carbon numbers larger than 12 and appear as an unresolved complex mixture on using traditional gas chromatography mass spectrometry (GC-MS) techniques (Presto et al., 2011). Early estimates of IVOC emissions and their SOA potential have significantly improved predictions of the SOA

formed from diesel exhaust (Jathar et al., 2014) and broadly, improved OA model performance in three-dimensional large-scale models (Murphy and Pandis, 2009; Pye and Seinfeld, 2010; Jathar et al., 2011; Tsimpidi et al., 2010). Very recently, Zhao et al. (2015) used a thermal desorption GC-MS to provide a detailed speciation of the carbon-number resolved linear, branched, and cyclic alkane IVOCs in diesel exhaust and found that these species accounted for up to 60% of the non-methane organic gas emissions; speciation in Zhao et al., (2015) was derived based on the carbon number, not the molecular structure. While IVOCs have been recognized as an important class of SOA precursors for diesel (and even for gasoline and biomass burning) sources, updated emission and speciation estimates from Zhao et al. (2015) have not been tested against observations of photochemically produced SOA from diesel exhaust.

Recently, several model frameworks have been developed to provide an improved representation of SOA formation that consider dimensions of SOA beyond just volatility. The statistical oxidation model (SOM) developed by Cappa and Wilson (2012) is one such example. The SOM is a semi-explicit, parameterizable mechanism that uses a two-dimensional carbon-oxygen grid to simulate the multigenerational chemistry and gas/particle partitioning of organic compounds. The SOM is semi-explicit in that it provides a statistical representation of the SOA composition, chemistry and thermodynamic properties. It is parameterizable in that parameters for a generalized chemical mechanism can be fit (e.g., probability of fragmentation) to reproduce measured data. Although the SOM does not explicitly track the product molecule's composition (e.g., functional groups), the carbon- and oxygen-number representation provides adequate detail to represent key atmospheric processes, e.g., reactions with oxidants, formation of functionalized

products, scission of carbon backbones or fragmentation, surface and condensed-phase chemistry and gas/particle partitioning. The two-dimensional VBS (2D-VBS) of Donahue et al. (2011) and the carbon-polarity grid of Pankow and Barsanti (2009) are examples of similar frameworks. These more sophisticated models have not yet been employed to study SOA formation from complex mixtures such as combustion emissions.

To summarize, energy and combustion sources (e.g., diesel engines) emit precursors that can photooxidize in the atmosphere to produce SOA. The SOA production is dependent not only on the precursor composition that could vary by combustion mode and fuel type and the photochemical age but affected by experimental artifacts (e.g., short condensation timescales) introduced through the use of oxidation flow reactors. There is, hence, a need to develop and apply sophisticated, yet computationally efficient, numerical models to simulate and study SOA formation from combustion emissions. In this work, we apply two different SOA model frameworks (VBS and SOM) to simulate the photochemical production of SOA in an OFR from diesel exhaust. The models are evaluated by comparing model predictions (OA and O:C) to the recent measurements made by Jathar et al. (2017) where SOA production was quantified for different photochemical ages under varying engine loads, fuels and aftertreatment devices. Both models accounted for: (i) semi-volatile and reactive POA, (ii) NO_x-dependent SOA production from IVOCs and VOCs, (iii) multi-generational aging, and (iv) kinetic gas/particle partitioning. The model-measurement comparison is used to highlight the importance of modeling the kinetic gas/particle partitioning of SOA in OFRs, the contribution of IVOCs to the total SOA production, and the ability of the SOM to accurately track the composition of SOA.

METHODS

2.1 EXPERIMENTS AND DATA

Jathar et al. (2017) performed photooxidation experiments using an OFR to measure SOA production from the exhaust of a 4.5L, John Deere diesel engine; the stock engine met Tier 3 emissions standards for non-road diesel engines. The OFR used herein was described in detail by Lambe et al. (2011) and the experimental setup and OA measurements from these experiments are described in detail by Jathar et al. (2017). To provide context for our modeling, we have very briefly summarized the experimental setup, measurements, and findings. Diesel exhaust was diluted by a factor of 45-110 before being pulled through an OFR. The intensity of the mercury lamps inside the OFR was varied to produce different hydroxyl radical (OH) concentrations and simulate different photochemical exposures. OFR used in the Jathar et al., 2017 was operated at wavelengths 185 and 254 nm. A suite of instrumentation was used to measure gas- (CO_2, CO, total hydrocarbons, NO_x, O_2, oxygenated organic compounds) and particle- (aerosol size and composition) phase concentrations. A total of fourteen experiments (see Table 1 for more details) were performed at varying engine loads, fuels and aftertreatment configurations (DPF: diesel particulate filter, designed to remove diesel particulate matter or soot from the exhast and DOC: diesel oxidation catalyst, designed to oxidize gas-phase hydrocarbons) where the OH exposure was varied between 0 and a maximum of 9.2×10^7 molecules-hr cm^{-3} (or equivalent to 2 days of photochemical aging at an OH concentration of 1.5×10^6 molecules cm^{-3}). On average, each experiment included sub-experiments at 6-7 different photochemical exposures. Jathar et al. (2017) quantified the mass concentrations and elemental composition of the POA (measured when OFR lights were off) and SOA (at varying OH exposures) as measured by the high-

resolution aerosol mass spectrometer (HR-AMS) and Friedman et al. (in preparation) quantified the gas-phase concentrations of oxygenated organic compounds as measured by the acetate reagent ion-based chemical ionization mass spectrometer (CIMS). At all engine configurations, SOA production more than exceeded the POA emissions after the equivalent of a few hours of atmospheric photochemical aging. SOA production was particularly strong at idle (or less fuel-efficient) engine loads and/or when exhaust temperatures were low and the aftertreatment's function may have been limited. Further, POA emissions and SOA production were nearly identical between diesel and biodiesel fuels. A synopsis of the THC (that includes all SOA precursors), POA, SOA, O:C, OH, and size distribution data is presented in Table 1.

Table 1: Primary emissions of THC and POA, maximum photochemical production of SOA, maximum O:C of the OA, maximum OH exposure, and size distribution data.

Load-Fuel-Aftertreatment Experiment	***Date***	***THC ($\mu g\ m^{-3}$)***	***POA ($\mu g\ m^{-3}$)***	***SOA$^{\#}$ ($\mu g\ m^{-3}$)***	***O: C#***	***OH$^{\#}$ (molec.-hr cm^{-3})***	***Surf. Area Mean Dia.* (nm)***	***Number Conc.$^{\&}$ (# cm^{-3})***
Idle-Diesel-None	June 3 June 5 June 12	1519 1810 2554	38±15 35±11 85±17	209±66 875±288 877±277	0.23±0.01 0.46±0.07 0.57±0.09	2.1×10^{7} 6.67×10^{7} 3.61×10^{7}	67	3.73×10^{5}
Idle-Biodiesel-None	June 4 June 8	1118 2160	22±12 69±20	999±316 1415±468	0.52±0.07 0.36±0.03	9.17×10^{7} 4.72×10^{7}	67$^{@}$	$3.73\times10^{5}$$^{@}$
Load-Diesel-None	June 3 June 5	959 711	19±11 37±13	181±58 253±100	0.37±0.01 0.32±0.04	3.6×10^{7} 2.61×10^{7}	75	5.38×10^{5}
Load-Biodiesel-None	June 4 June 8	1634 518	29±18 46±22	645±204 284±106	0.38±0.05 0.30±0.04	2.78×10^{7} 1.42×10^{7}	75$^{@}$	$5.38\times10^{5}$$^{@}$
Idle-Diesel-DPF+DOC*	June 9	2135	1.5±0.6	1040±335	0.37±0.02	5×10^{7}	65	630
Load-Diesel-DPF+DOC*	June 9	303	1.6±	146±48	0.29±0.01	1.31×10^{7}	75	963
Idle-Biodiesel-DPF+DOC*	June 10	1773	2.6±1	787±250	0.44±0.04	5.28×10^{7}	65$^{@}$	630$^{@}$
Load-Biodiesel-	June 10	261	2±0.14	107±9	0.29±0.01	1.39×10^{7}	75$^{@}$	963$^{@}$

DPF+DOC*								

DPF=diesel particulate filter, DOC=diesel oxidation catalyst
#maximum values measured in each experiment
**values measured at no OH exposure in each experiment*
@No data, assumed to be similar to the equivalent diesel experiment

2.2 ORGANIC AEROSOL MODELS

In this work, we use two different OA models to predict the mass concentrations and chemical composition of SOA and compare predictions against the SOA measurements from Jathar et al. (2017) and Friedman et al. (in preparation). In this section, we briefly describe the two model frameworks, namely the Volatility Basis Set and the Statistical Oxidation Model, used to simulate the coupled chemistry, thermodynamic properties, and gas/particle partitioning of OA.

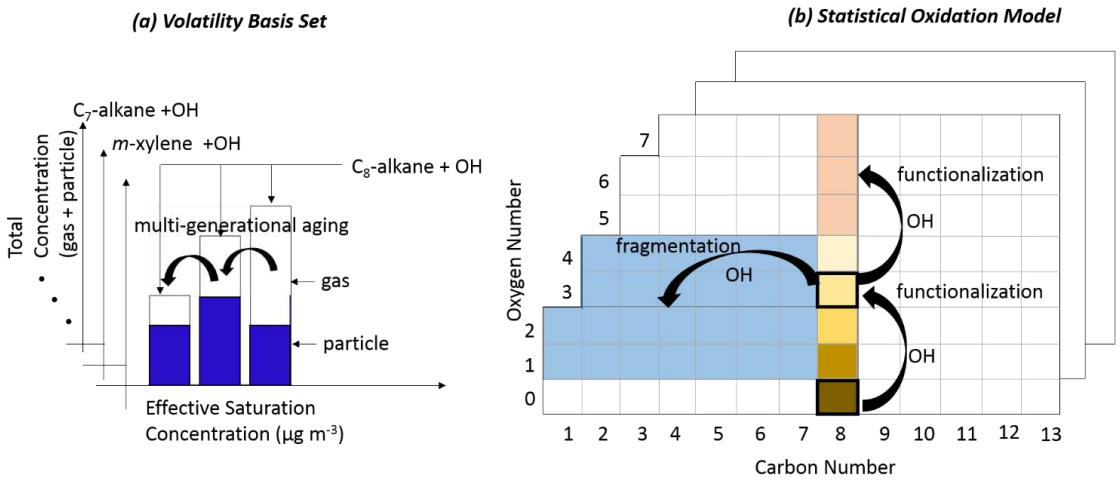

Figure 1: Schematic of the (a) VBS and (b) SOM model frameworks to model the VOC oxidation, product formation/loss, thermodynamic properties, and gas/particle partitioning of POA and SOA. In the VBS model, benzene reacts with the OH radical to form three oxidation products. In the SOM, a hydrocarbon with carbon number 8 (highlighted) reacts with the OH radical to form four functionalized products with 1 to 4 oxygens. One of the products reacts with OH to either form four new functionalized products or fragment into smaller products.

2.2.1 VOLATILITY BASIS SET (VBS)

The Volatility Basis Set (VBS) model, developed by Donahue et al. (2006), is a parameterizable model that allows for a volatility-based representation of the coupled chemistry, thermodynamic properties, and gas/particle partitioning of OA. The VBS uses logarithmically spaced basis sets based on the effective saturation concentration (C^*); C^* of a species determines the partitioning between the gas and particle phases (Pankow et al., 1994). In the VBS model, VOCs are allowed to react with OH to yield a unique product distribution in C^* space that represents stable first-generation products. Subsequent gas-phase oxidation or so-called 'aging' of the VBS products was modeled using the scheme of Robinson et al. (2007) where reaction of the precursor with OH was assumed to yield a product with a C^* that is an order of magnitude lower than the precursor. This scheme does not consider fragmentation reactions. The following equations are used to represent the VOC oxidation (equation 1) and formation of products from VOC oxidation and aging reactions (equation 2):

$$\frac{dV_i}{dt} = -k_{OH,i}[V_i][OH] \quad (1)$$

$$\frac{dC_{i,j}^{g+p}}{dt} = \alpha_{i,j}k_{OH,i}[V][OH] + \beta k_{OH,aging}[C_{i,j+1}^{g}][OH] - \gamma k_{OH,aging}[C_{i,j}^{g}][OH] \quad (2)$$

Where V_i is the i^{th} VOC (μg m^{-3}; here, VOC includes VOCs, IVOCs and SVOCs), $k_{OH,i}$ (cm^3 mol^{-1} s^{-1})is the reaction rate constant between the i^{th} VOC and *OH*, $C_{i,j}^{g+p}$ is the gas + particle-phase concentration of the i^{th} VOC in the j^{th} bin,$\alpha_{i,j}$is the mass yield of the first-generation oxidation product of the i^{th} precursor of the j^{th} bin (Table 2), $k_{OH,aging}$ is the reaction rate constant to represent multi-generational aging of the oxidation products, and $\beta$and $\gamma$are the mass yields associated with the production and loss terms from multi-generational aging. For the j^{th} bin, the second term in equation (2) represents the formation of oxidation products from the $j+1^{th}$

volatility bin and the third term in equation (2) represents the loss of precursor from the j^{th} bin. β and γ are assumed to have a value of 1 (meaning no fragmentation) but are zero for the last and the first bins respectively.

The condensation (or mass transfer) of the VBS products to the particle phase was assumed to be kinetically-limited in the oxidation flow reactor (Jathar et al., 2017; Palm et al., 2016); Section 2.3 describes the condensation/evaporation equation used to model kinetic gas/particle partitioning. Product distributions for 2 different VOCs for C^* bins ranging from 10^{-2} to 10^6 µg m^{-3} were refit based on parameterizations published in the literature; VOCs, their VBS mass yields, and the relevant references are listed in Table 2. Each VOC species in the emissions was assigned a surrogate from Table 2 to model SOA formation in the VBS model. The higher(C_{12}-C_{22}) branched and cyclic alkanes were assigned surrogates of linear alkanes. For example, C_{12} branched alkane was given a surrogate of C_{10} linear alkane and for C_{12} cyclic alkane, C_{14} linear alkane was given as surrogate. Since we have mass yields up to *n*-heptadecane only, we considered *n*-heptadecane as surrogates for alkanes C_{17}-C_{22}.

Table 2: SOA precursors and VBS mass yields used in the VBS model.

Species	***$log_{10}C^*$***					***Reference***
	0.1	***1***	***10***	***100***	***1000***	
toluene	0.0000	0.0100	0.2400	0.4500	0.7000	Hildebrandt et al.,2009
benzene	0.0392	0.0315	0.0000	0.8230	0.0957	Ng et al., 2007
m-xylene	0.0032	0.0106	0.0633	0.0465	0.0000	Ng et al., 2007
p-xylene	0.0000	0.0022	0.0764	0.0000	0.0000	Song et al.,2007
o-xylene	0.0000	0.0132	0.1140	0.0000	0.0000	Song et al.,2007
naphthalene	0.0000	0.1660	0.0000	0.5400	0.8130	Chan et al.,2009
1-methylnaphthalene	0.0000	0.0170	0.4860	0.0000	0.0000	Chan et al.,2009
2-methylnaphthalene	0.0000	0.0531	0.5040	0.0000	0.0000	Chan et al.,2009
1,2-dimethylnaphthalene	0.0000	0.3100	0.0000	0.0000	0.0000	Chan et al.,2009

1-methyl-3-*n*-propylbenzene	0.0000	0.0000	0.0405	0.0694	0.1140	Odum et al.,1997?
n-decane	0.0000	0.0000	0.0110	0.1280	0.2420	Presto et al.,2010*
n-undecane	0.0000	0.0040	0.0720	0.1760	0.1450	Presto et al.,2010*
n-dodecane	0.0000	0.0140	0.1100	0.1600	0.0000	Presto et al.,2010
n-tridecane	0.0140	0.0590	0.0940	0.0710	0.0000	Presto et al.,2010
n-tetradecane	0.0940	0.3000	0.3500	0.0000	0.0000	Presto et al.,2010
n-pentadecane	0.0440	0.0710	0.4100	0.3000	0.0000	Presto et al.,2010
n-hexadecane	0.0530	0.0830	0.4600	0.2500	0.0000	Presto et al.,2010
n-heptadecane	0.0630	0.0890	0.5500	0.2000	0.0000	Presto et al.,2010

* estimated from the Presto et al. (2010) data

2.2.2 STATISTICAL OXIDATION MODEL (SOM)

The Statistical Oxidation Model (SOM), developed by Cappa and Wilson (2012) is a semi-explicit, parameterizable model that allows for a statistical representation of the coupled chemistry, thermodynamic properties, and gas/particle partitioning of OA; the SOM does not explicitly track functional groups or molecular structure. The SOM uses a 2-dimensional carbon-oxygen grid to track gas- and particle-phase precursors and products from VOC oxidation. Each cell in the SOM grid represents a model organic species with a molecular weight defined by the formula $C_xH_yO_z$. A SOM species reflects the average properties (e.g. C^*, reactivity) of all actual species with the same number of carbon (N_C) and oxygen (N_O) atoms that are produced from a given precursor class (e.g., aromatics, alkanes). In the SOM, all gas-phase species are assumed to be reactive towards OH and the OH reactivity (k_{OH}) is calculated using equation 3 as follows:

$$log(k_{OH}) = A_1 + A_2 \times (N_C^{A_S}) \times exp(-1 \times \frac{E_a}{8.314 \times T}) \times [1 + \frac{b_1}{\sigma\sqrt{2\pi}} exp(-\frac{1(ln(N_O+0.01)-ln(b_2)^2}{2\sigma^2})] \quad (3)$$

$$\sigma\ (N_C \leq 15) = 0.0214 \times N_C + 0.5238$$

$$\sigma\ (N_C \geq 15) = -0.115 \times N_C + 2.695$$

$$b_1 = -0.2583 \times N_C + 5.8944$$

$$b_2\ (N_C \leq 15) = 0.0314 \times N_C + 0.9871;\ b_2\ (N_C > 15) = 0.25 \times N_C - 2.183$$

Where A_1=15.1, A_2=3.94, and A_3=0.797. k_{OH} for a specified N_C and N_O is assumed to be the same for species in all the SOM grids.

The reactions with OH lead to either functionalization or fragmentation, resulting in movement through the carbon-oxygen grid. Six precursor-specific adjustable parameters are assigned for each SOM grid: four parameters that define the molar yields of the four functionalized, oxidized products ($p_{O,k}$, $\Sigma p_{O,k}=1$), one parameter that determines the probability of functionalization or fragmentation (P_{Frag},, P_{Func}=1-P_{Frag}) and one parameter that describes the change in C^* associated with the addition of one oxygen atom (ΔLVP). The following equation represents the evolution of species in the SOM grid.

$$\frac{d[C_X O_Z]}{dt} = -k_{OH}^{X,Z}[OH][C_X O_Z],$$

$$+[OH]\sum_{k=1}^{4} k_{OH}^{X,Z-k} P_{func}^{X,Z-k} p_{O,k}[C_X O_{Z-k}] + [OH]\sum_{j=1}^{j_{max}}\sum_{k=0}^{k_{max}-Z} k_{OH}^{X+j,Z-1+k}\frac{P_{frag}^{X,Z-1+k}}{N_{fragments}^{X,Z}}[C_X O_{Z-1+k}]$$

(5)

where $C_X O_Z$ is the SOM species with X carbon atoms and Z oxygen atoms and $N_{fragments}$ is the SOM species specific number of possible fragments. The probability of fragmentation is modeled using equation 6 as a function of the O:C ratio because higher O:C ratio compounds are expected to have a higher probability of fragmentation (Chacon-Madrid and Donahue, 2011):

$$P_{frag} = \left(\frac{N_O}{N_C}\right)^{m_{frag}} \quad (6)$$

The C^* for each SOM species is calculated using equation 7 as follows:

$$log_{10}C^* = -0.337MW_{HC} + 11.56 - (N_O \times \Delta LVP) \quad (7)$$

Where MW_{HC} is the molecular weight of the hydrocarbon backbone (accounting only for the carbon and hydrogen atoms) and ΔLVP is change in the C^* associated with the addition of one oxygen atom. The parameters used to model SOA formation from VOCs in this work are based on those published in Jathar et al. (2015) and are listed in Table 3. Each VOC species in the emissions was assigned a surrogate from Table 3 to model SOA formation in the SOM model. However, unlike the VBS where the SOA mass yield between the VOC species and the surrogate is identical, the surrogate in the SOM model defines the statistical pathway for multi-generational oxidation and could very likely have different SOA mass yields than the VOC species.

Table 3: SOA precursors and parameters used in the SOM model.

Species	m_{frag}	ΔLVP	$p_{O,1}$	$p_{O,2}$	$p_{O,3}$	$p_{O,4}$	***Primary Reference***
n-dodecane	0.0980	1.3900	0.9270	0.0101	0.0180	0.0445	Loza et al. (2014)
methylundecane	0.0100	1.2100	0.7419	0.0011	0.1820	0.0750	Loza et al. (2014)
hexylcyclohexane	0.0477	1.5700	0.7313	0.0381	0.2101	0.0205	Loza et al. (2014)
toluene	0.2220	1.2400	0.0029	0.0010	0.0010	1.0100	Zhang et al. (2014)
benzene	0.5350	1.7000	0.0792	0.0010	0.9190	0.0010	Ng et al. (2007)
m-xylene	0.0100	1.6800	0.9360	0.0010	0.0021	0.0609	Ng et al. (2007)
naphthalene	0.1210	1.3100	0.6440	0.0010	0.0460	0.3080	Chan et al. (2009)

2.3 KINETIC GAS-PARTICLE PARTITIONING

Palm et al. (2016) and Jathar et al. (2017) have argued that the short residence times in the OFR may not permit all low-volatility products formed from VOC oxidation to condense onto

preexisting aerosol. Hence, unlike earlier work that has assumed equilibrium partitioning to model OFR-produced OA (Tkacik et al., 2014, Chen et al., 2013), we model the kinetic partitioning of OA using equation 9 (Zhang et al., 2014):

$$\frac{dC_{i,j}^{p}}{dt} = 2\pi D_j D_p N_p F_{FS}(C_{i,j}^{g} - \frac{C_{i,j}^{p} C_j^*}{C_{OA}}) \quad (9)$$

Where $C_{i,j}^{p}$ is the particle-phase mass concentration for the i^{th} VOC and j^{th} organic species, D_j is the gas-phase diffusion coefficient of the j^{th} organic species, D_p is the number mean particle diameter, N_p is the total particle number concentration, F_{FS} is Fuchs-Sutugin correction for non-continuum mass transfer, $C_{i,j}^{g}$ is the gas-phase mass concentration for the i^{th} VOC and j^{th} organic species, C_j^* is the effective saturation concentration of the j^{th} organic species, and C_{OA} is the total OA mass concentration. The prefix $2\pi D_j D_p N_p F_{FS}$ is referred to later as the condensation sink. The j^{th} organic species refers to the organic compounds tracked in the VBS bins and the SOM grids. The gas-phase diffusion coefficient is calculated for each organic species as follows:

$$D_j = D_{CO_2} \frac{MW_{CO_2}}{MW_j} \quad (10)$$

Where D_{CO_2} is the gas-phase diffusion coefficient of CO_2 (1.38×10^{-5} m^2 s^{-1}), MW_{CO_2} (g mole^{-1}) is the molecular weight of CO_2, and MW_j (g mole^{-1}) is the molecular weight of the j^{th} species. In the VBS model where the SOA is anonymized, we assume all condensing species to have a molecular weight of 300 g mole^{-1}; we test the sensitivity of this assumption on model predictions. The Fuchs-Sutugin correction is calculated as follows:

$$F_{FS} = \frac{0.75\alpha(1+Kn)}{Kn^2+Kn+0.283\cdot Kn\cdot\alpha+0.75\alpha} \quad (11)$$

$$Kn = \frac{2\lambda_j}{D_p} \quad (12)$$

$$\lambda_j = \frac{3D_j}{C_j} \quad (13)$$

$$C_j = \sqrt{\frac{8N_A kT}{\pi MW_j}} \quad (14)$$

Where *Kn* is the Knudsen number, α is the mass accommodation coefficient, λ_j is the mean free path of the j^{th} organic species in air (m), C_j is the root mean square speed of the gas (m s^{-1}), N_A is Avogadro's Number, *k* is Boltzmann constant (m^2 kg s^{-2} K^{-1}) and *T* is the temperature (K).

2.4 MODEL INPUTS

2.4.1 SEMI-VOLATILE AND REACTIVE POA

Jathar et al. (2017) measured emissions of POA at no OH exposure and these measured concentrations were used to initialize the preexisting OA available for absorptive partitioning in the model simulations. Previous work has conclusively shown that POA is semi-volatile and exists in an equilibrium with gas-phase vapors (Robinson et al., 2007; May et al., 2013a,b,c); POA and its vapors are hereafter collectively referred to as primary organic carbon (POC). Mass concentrations of the POC vapors were determined by assuming that the POC mixture in the experiments modeled in this work was consistent with the normalized, volatility-resolved distribution of POC products estimated by May et al. (2013) from a suite of on- and off-road diesel vehicles. The volatility distribution of May et al. (2013) for diesel POC is listed in Table 4(a). For the SOM, we assumed that the POC could be represented using a distribution of *n*-alkanes and we refit the volatility distribution in Table 4(a) to develop a carbon-number resolved distribution of *n*-alkanes; this distribution is listed in Table 4(b). The POA and POC vapors estimated for the VBS and SOM models for all the experiments are listed in supplementary information.

Table 4: (a) Volatility- and (b) carbon-number resolved distributions used to determine mass concentrations of POC vapors in the VBS and SOM models

C^* ($\mu g\ m^{-3}$)	10^{-2}	10^{-1}	10^{1}	10^{2}	10^{3}	10^{4}	10^{5}	10^{6}
f_i	0.03	0.25	0.37	0.23	0.06	0.03	0.01	0.01

Carbon No.	<16	16	17	18	19	20	21	22	23	24	25	26	>26
f_i	0.003	0.000	0.058	0.043	0.055	0.094	0.146	0.181	0.178	0.137	0.078	0.026	0.001

2.4.2 SOA PRECURSOR EMISSIONS

Jathar et al. (2017) did not speciate the THC (that includes the SOA precursors) emissions for the different tests and hence we had to develop our own emissions profiles based on previously published literature to speciate the THC emissions. In this work, we used four different emissions profiles listed in EPA SPECIATE version 4.3 that are commonly used to speciate THC emissions from diesel engines for emission inventories used in atmospheric modeling (Woody et al., 2016): Profile #s 3161 (Diesel Exhaust- Farm Equipment), #8777 (Heavy duty diesel exhaust), 4777 (Biodiesel Exhaust- Light Duty) and 4771 (Biodiesel Exhaust - Light Duty). Profile #3161 best matches the diesel engine source and diesel fuel used by Jathar et al.,2017 and was used as the baseline emissions profile to speciate THC emissions; we examined the sensitivity of using Profile #8774 on model predictions. Profile #4777 was used as the baseline emissions profile to speciate THC emissions for tests performed using the biodiesel fuel and we used Profile #4771 to test sensitivity to model predictions. We were unable to find a comprehensive emissions profile for THC emissions from the use of straight biodiesel fuel (as used by Jathar et al. (2017)) in the literature and hence we had to rely on emissions profiles that were determined for biodiesel-diesel blends.

Prior work in studying SOA formation has revealed that traditional speciation of THC emissions does not include emissions of high molecular-weight organic compounds such as IVOCs that are important SOA precursors (Jathar et al., 2014). In Profile #3161 and #8774 these are partially accounted for in the 'unknown' species category. Zhao et al. (2015) recently estimated the magnitude of IVOC emissions in THC emissions found in a suite of on- and off-road diesel engines and provided a semi-explicit speciation of the IVOC emissions as a carbon-number distribution of linear, branched and cyclic alkanes. To account for these IVOC emissions, we assumed that the baseline emissions profiles contained 60% (based on the median estimate in Zhao et al. (2015)) IVOCs on a mass-basis. We performed sensitivity simulations using 0% (assuming that the THC emissions contained no IVOCs) and 13.6% (based on the 'unknown' category in Profile #3161) IVOCs on a mass-basis. Addition of IVOCs to the baseline emissions profile meant that the traditional species had to be renormalized to accommodate the IVOCs. Table 5 lists the normalized baseline emissions profiles for SOA precursors used for diesel and biodiesel exhaust with 60% IVOCs including the reaction rate constants with *OH* (k_{OH}) and surrogates (or model compound) used to model SOA formation for the VBS and SOM models. Concentrations for each species for any experiment were determined by simply multiplying the THC mass concentrations with the normalized emissions profile.

Table 5: Mass fraction, VBS and SOM surrogates for SOA forming precursors

Species	***k_{OH} (cm^3 $molecules^{-1}$ s^{-1})***	***Mass Fraction***		***VBS Surrogate***	***SOM Surrogate***
		Diesel	***Biodiesel***		
ethylbenzene	7.0E-12	0.144	0.071	toluene	toluene
indan	1.9E-11	0.087	-	naphthalene	naphthalene
butylbenzene	4.5E-12	0.065	0.405	*m*-xylene	*m*-xylene

diethylbenzene	8.11E-12	0.101	-	*m*-xylene	*m*-xylene
isopropyltoluene	8.54E-12	-	0.308	toluene	toluene
m-xylene	2.31E-11	0.282	0.318	*m*-xylene	*m*-xylene
o-xylene	1.36E-11	0.157	0.338	*o*-xylene	*m*-xylene
p-xylene	1.43E-11	0.046	-	*p*-xylene	*m*-xylene
n-decane	1.1E-11	0.245	1.460	decane	Decane
n-undecane	1.23E-11	0.120	1.660	undecane	Undecane
toluene	5.63E-12	1.405	0.680	toluene	Toluene
n-tridecane	1.68E-11	-	0.525	tridecane	tridecane
benzaldehyde	1.2E-11	0.324	-	benzene	benzene
benzene	1.22E-12	0.925	1.370	benzene	benzene
C_{10} aromatics	2.3E-11	0.037	-	*m*-xylene	*m*-xylene
C_9 aromatics	2.31E-11	0.230	-	*m*-xylene	*m*-xylene
1,2,3-trimethylbenzene	3.27E-11	0.056	-	*m*-xylene	*m*-xylene
1,2,4-trimethylbenzene	3.25E-11	0.245	0.404	*m*-xylene	*m*-xylene
1,2-diethylbenzene	8.11E-12	0.041	-	toluene	toluene
1,3,5-trimethylbenzene	5.67E-11	-	0.162	*m*-xylene	*m*-xylene
1,2-dimethyl-4-ethylbenzene	1.69E-11	-	0.176	*m*-xylene	*m*-xylene
1,3-dimethyl-2-ethylbenzene	1.76E-11	-	0.283	*m*-xylene	*m*-xylene
1,4-dimethyl-2-ethylbenzene	1.69E-11	-	0.370	*m*-xylene	*m*-xylene
1-(1,1-dimethylethyl)-3,5-dimethylbenzene	3.01E-11	-	0.318	*m*-xylene	*m*-xylene
1-methyl-2-ethylbenzene	7.44E-12	0.065	0.328	toluene	toluene
1-methyl-3-ethylbenzene	1.39E-11	0.116	0.616	toluene	toluene
1-methyl-2-tert-butylbenzene	6.74E-12	-	0.369	toluene	toluene
1-tert-butyl-4-ethylbenzene	7.42E-12	-	0.166	*m*-xylene	*m*-xylene
2-methyl-butyl-benzene	1.02E-11	-	0.945	*m*-xylene	*m*-xylene

3,3-dimethyloctane	7.21E-12	-	0.262	decane	C_{10} branched alkane
3-ethyloctane	1.18E-11	-	0.162	decane	C_{10} branched alkane
3-methylnonane	1.14E-11	-	0.227	decane	C_{10} branched alkane
C_{12} branched alkane	1.82E-11	2.268	2.268	decane	decane
C_{13} branched alkane	1.68E-11	1.623	1.623	undecane	undecane
C_{14} branched alkane	1.39E-11	1.052	1.052	dodecane	dodecane
C_{15} branched alkane	1.82E-11	0.939	0.939	tridecane	tridecane
C_{16} branched alkane	1.96E-11	0.988	0.988	tetradecane	tetradecane
C_{17} branched alkane	2.1E-11	0.440	0.440	pentadecane	pentadecane
C_{18} branched alkane	2.24E-11	0.573	0.573	hexadecane	hexadecane
C_{19} branched alkane	2.38E-11	0.343	0.343	heptadecane	heptadecane
C_{20} branched alkane	2.52E-11	0.194	0.194	heptadecane	heptadecane
C_{21} branched alkane	2.67E-11	0.128	0.128	heptadecane	heptadecane
C_{22} branched alkane	2.81E-11	0.121	0.121	heptadecane	heptadecane
C_{12} cyclic alkane	1.82E-11	8.690	8.690	tetradecane	tetradecane
C_{13} cyclic alkane	1.68E-11	8.858	8.858	pentadecane	pentadecane
C_{14} cyclic alkane	1.39E-11	6.299	6.299	hexadecane	hexadecane
C_{15} cyclic alkane	1.82E-11	5.723	5.723	heptadecane	heptadecane
C_{16} cyclic alkane	1.96E-11	4.372	4.372	heptadecane	heptadecane
C_{17} cyclic alkane	2.1E-11	3.711	3.711	heptadecane	heptadecane
C_{18} cyclic alkane	2.24E-11	3.382	3.382	heptadecane	heptadecane
C_{19} cyclic alkane	2.38E-11	2.115	2.115	heptadecane	heptadecane
C_{20} cyclic	2.52E-11	1.181	1.181	heptadecane	heptadecane

alkane					
C_{21} cyclic alkane	2.67E-11	0.748	0.748	heptadecane	heptadecane
C_{22} cyclic alkane	2.81E-11	0.629	0.629	heptadecane	heptadecane
dodecane	1.82E-11	1.167	1.167	dodecane	dodecane
tridecane	1.68E-11	1.094	1.094	tridecane	tridecane
tetradecane	1.39E-11	0.730	0.730	tetradecane	tetradecane
pentadecane	1.82E-11	0.613	0.613	pentadecane	pentadecane
hexadecane	1.96E-11	0.456	0.456	hexadecane	hexadecane
heptadecane	2.1E-11	0.331	0.331	heptadecane	heptadecane
octadecane	2.24E-11	0.296	0.296	heptadecane	heptadecane
nonadecane	2.38E-11	0.145	0.145	heptadecane	heptadecane
eicosane	2.52E-11	0.073	0.073	heptadecane	heptadecane
heneicosane	2.67E-11	0.044	0.044	heptadecane	heptadecane
docosane	2.81E-11	0.029	0.029	heptadecane	heptadecane
pristane	2.44E-11	0.287	0.287	heptadecane	C_{19} branched alkane
phytane	2.61E-11	0.160	0.160	heptadecane	C_{20} branched alkane
naphthalene	2.3E-11	0.208	0.208	naphthalene	naphthalene
phenanthrene	1.3E-11	0.024	0.0235	naphthalene	naphthalene

2.4.3 PARTICLE SIZE DISTRIBUTION

For the sake of numerical simplicity, we considered a monodisperse size distribution to model the kinetic gas/particle partitioning. Model simulations were initialized with the surface area mean diameter and number concentration measured by Jathar et al. (2017) at no OH exposure for the non-DPF+DOC experiments. We used the OH-specific surface area mean diameter-number concentration pairs for the DPF+DOC experiments. The rationale for this is discussed in Section 3.5.3. The condensing SOA mass was used to calculate the change in particle size but the number concentration was conserved. These data are listed in Table 1. We also examined the sensitivity of different particle size distribution inputs on model predictions.

2.5 MODEL SIMULATIONS

The VBS and SOM models were run separately for each photochemical exposure simulated for each experiment listed in Table 1. We assumed that as the diluted exhaust mixture traveled from one end to the other of the OFR over a period of 100 seconds, the mixture was exposed to a constant OH concentration that oxidized the mixture to form SOA. The constant OH concentration was calculated by dividing the OH exposure estimated by Jathar et al. (2017) by 100 seconds. In each VBS model simulation, POC was tracked in a separate basis set while products from each SOA precursor were tracked in separate basis sets. In each SOM model simulation, we only tracked the SOM grid of the surrogate instead of tracking each precursor. Model simulations were performed in phases to answer specific questions. First, we performed simulations with the VBS and SOM models using a base set of inputs for one of the Diesel-Idle-None experiments. Our base set of inputs included: Profile #3161 for diesel experiments and Profile #4777 for biodiesel experiments, a 60% IVOC mass fraction, kinetic gas/particle partitioning with a mass accommodation coefficient of 0.1, and particle size calculated using the surface area mean diameter. These simulations provided a general overview of the model predictions. Second, we performed simulations with the VBS model assuming equilibrium and kinetic gas/particle partitioning for the Diesel-Idle-None experiment performed on June 5. These were performed to examine the validity of the equilibrium gas/particle partitioning assumption to model OFR data. Third, we performed simulations with the VBS and SOM models with different IVOC mass fractions for all the experiments listed in Table 1. These allowed us to investigate the importance of IVOCs to model the formation and, in case of the SOM, model the elemental composition of the SOA. Finally, we performed simulations with the VBS and SOM models to explore the sensitivity of the model predictions to the following key inputs: IVOC

parameterization, choice of emissions profile, particle size distribution inputs, vapor wall losses and molecular weight of the condensing species in the VBS model. Model runtime of SOM (in Igor version) is 500 seconds and VBS (in MATLAB) is 10 seconds in an Intel 4^{th} generation i5 processor at 1.7GHz.

RESULTS

3.1 GENERAL RESULTS

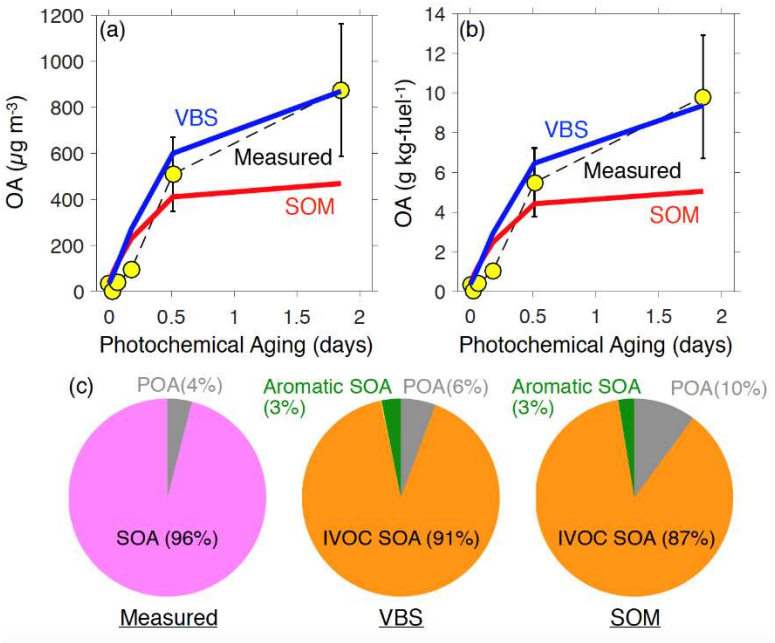

Figure 2: VBS and SOM model predictions of OA when run assuming the base case inputs compared to measurements from the experiment performed on June 5(Diesel-Idle-None) as a function of photochemical age. Panel (a) has comparisons in µg m^{-3} and panel (b) has comparisons in g kg-$fuel^{-1}$. Panel (c) shows the modeled and measured OA composition at the highest photochemical exposure.

We compare predictions of OA from the VBS and SOM models to the measurements in Figure 2 for the Diesel-Idle-None experiment performed on June 5. Figures 2(a) and 2(b) compare predictions to the measurements in units of µg m^{-3} and g kg-$fuel^{-1}$ respectively; hereafter we present all OA mass predictions in units of g kg-$fuel^{-1}$. Figure 2(c) compares the VBS and SOM predicted composition of OA at the maximum photochemical exposure to the measured composition of OA. The VBS and SOM models seemed to slightly overpredict the OA evolution at photochemical exposures lower than half a day. For photochemical exposures larger than half a day, the VBS model performed very well in reproducing the OA evolution but the SOM

underpredicted the OA mass by about a factor of two at the highest photochemical exposure. The overprediction by both models at lower photochemical ages and the underprediction by the SOM at higher photochemical ages can be attributed to the choice and uncertainty in the various inputs for the two models. These assumptions and inputs will be explored in the sections below. The VBS and SOM models predicted that the OA at the maximum photochemical exposure was dominated (90-94%) by SOA produced from VOC and IVOC oxidation, which agreed well with the measured composition. Furthermore, both models suggested that most of the SOA emanated from the oxidation of IVOCs with only about 3% resulting from the oxidation of aromatic VOCs and less than 1% resulting from C_{12} and lower alkane VOCs. This dominance of IVOCs in explaining the photochemically produced SOA is in line with previous studies that have modeled SOA formation from diesel exhaust (Tkacik et al., 2014; Jathar et al., 2014).

3.2 EQUILIBRIUM VERSUS KINETIC GAS/PARTICLE PARTITIONING

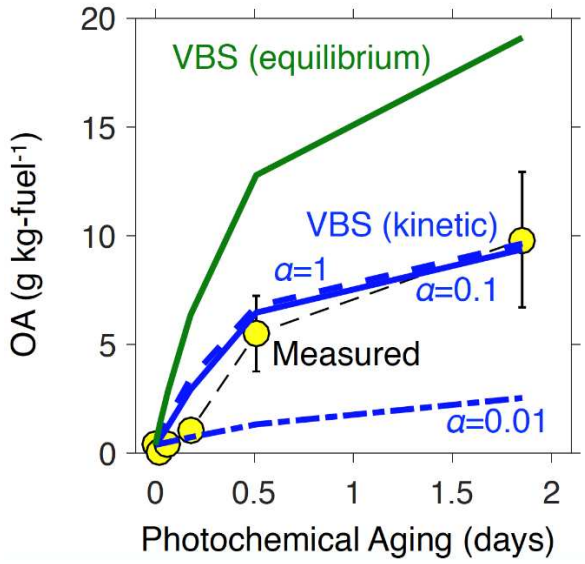

Figure 3: VBS model predictions of OA as a function of photochemical age assuming instantaneous equilibrium (green) and kinetic gas/particle partitioning (blue; run at three accommodation coefficients, α = 1(dashed) ,0.1(solid) and 0.01(dash-dot))

Large-scale models commonly assume instantaneous or equilibrium gas/particle partitioning since the timescales of other atmospheric processes (e.g., chemistry, transport, deposition) are typically much slower than those required for gases and sub-micron particles to achieve equilibrium (Meng and Seinfeld, 1996; Zhang et al., 2012). Hence, models applied to simulate SOA production in environmental chambers, and even in OFRs, have also assumed equilibrium partitioning. Here, we examine the validity of assuming equilibrium partitioning to model OFR data by performing model simulations assuming equilibrium and kinetic gas/particle partitioning and comparing model predictions against measurements from the Diesel-Idle-None experiment performed on June 5. The simulations were performed with the VBS model used in Section 2.1 using three different mass accommodation coefficients (α=0.01, 0.1, 1) to capture the uncertainty in modeling the kinetic gas/particle partitioning; the mass accommodation coefficient (α) is defined as the probability that the collision of a condensing molecule will result in mass transfer from the gas to the particle phases. We only used the VBS model here since it offered good comparison of model predictions against measurements for the experiment performed on June 5. Results from the simulations are shown in Figure 3. We find that the VBS model on assuming equilibrium partitioning significantly over-predicted the photochemical production of SOA by as much as a factor of two. This comparison indicates that assuming equilibrium partitioning to model OFR data will likely over-predict the condensation and formation of SOA. Additionally, the results suggest that the model predictions were relatively insensitive to α values of 0.1 and 1 but were dramatically lower (factor of ~4) for an α value of 0.01. Given the reasonable model-measurement comparison of the VBS model at an α value of 0.1 and 1, we argue that condensation in an OFR may not be well represented by an α value lower than 0.1.

3.3 INFLUENCE OF IVOCS ON SOA FORMATION

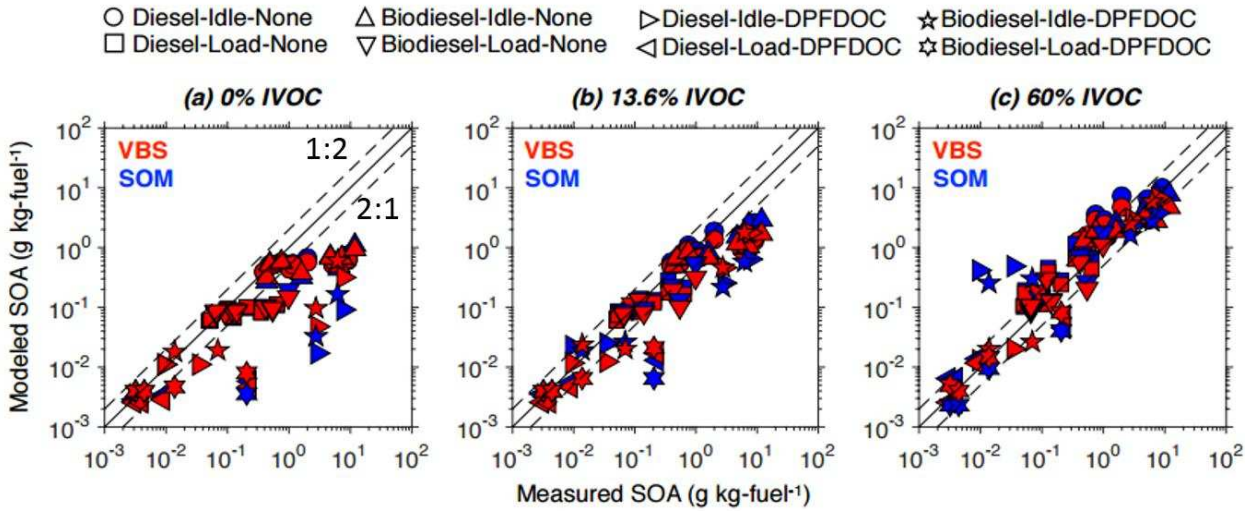

Figure 4: SOA Predictions from the VBS and SOM models assuming 0%, 13.6% and 60% IVOC mass fractions compared to measurements at α=0.1 with Zhao et al., (2015) speciation for IVOCs.

Previous work has shown that combustion-related IVOCs are important precursors of SOA (Robinson et al., 2007; Gordon et al., 2014 a,b; Jathar et al., 2014; Dzepina et al., 2009). In Figure 4, we use scatter plots to compare predictions of SOA from the VBS and SOM models against measurements for all the experiments listed in Table 1 and at all photochemical ages. The three panels in Figure 4 show model-measurement comparisons assuming three different fractions of IVOCs: 0%, 13.6% and 60%. The model performance is also captured using statistical metrics of fractional bias, fractional error (gives equal weight to underestimations and overestimations, fractional bias varies between +2 to -2 and has value zero for an ideal model), and R^2 in Table 6. Traditional emissions inventories rarely include IVOCs and hence the 0% case reflects the SOA treatment in traditional models. The 13.6% IVOC case reflects the unspeciated fraction listed in diesel exhaust emissions profiles, which is typically neglected by emissions models and not considered to form SOA. The 60% IVOC case reflects the latest estimate from

Zhao et al. (2015) based on measurements from on- and off-road diesel vehicles. The model-measurement comparison and the model skill was very poor when no IVOCs were included (fractional bias>70% and fractional error>73%). The model performance improved with 13.6% IVOCs (fractional bias>40% and fractional error>60%) but was better still with 60% IVOCs (fractional bias>15% and fractional error>35%) where there was very little bias in the model predictions. The optimal model performance that produced the lowest fractional bias and fractional error was found at an IVOC mass fraction of 40% (fractional bias=-4% and fractional error=48%). These comparisons indicate that it is critical that IVOCs be included when modeling the SOA formation from diesel exhaust. In Figure 5(a), we plot the relative contribution of precursors and POA to the OA mass at the highest photochemical exposure for all the experiments and we also plot the precursor mass fractions for all the experiments in figure 5(b). Cyclic alkane IVOCs were found to contribute the most (40-75%) to SOA formation. Since the speciation of cyclic alkane IVOCs in Zhao et al. (2015) did not include any specificity in terms of the molecular structure and that the parameterizations to model SOA formation from cyclic alkane IVOCs for both models was non-specific (in the VBS model the surrogate for a cyclic alkane IVOC was determined through equivalence with a straight alkane IVOC; in the SOM model the cyclic alkane IVOCs were tied to parameterizations for hexylcyclohexane), the SOA predictions from the oxidation of cyclic alkane IVOCs are relatively uncertain. We recommend that future work focus on more detailed speciation of the cyclic alkane IVOCs as well as on chamber experiments on those speciated compounds to improve quantification of their SOA mass yields.

(a)

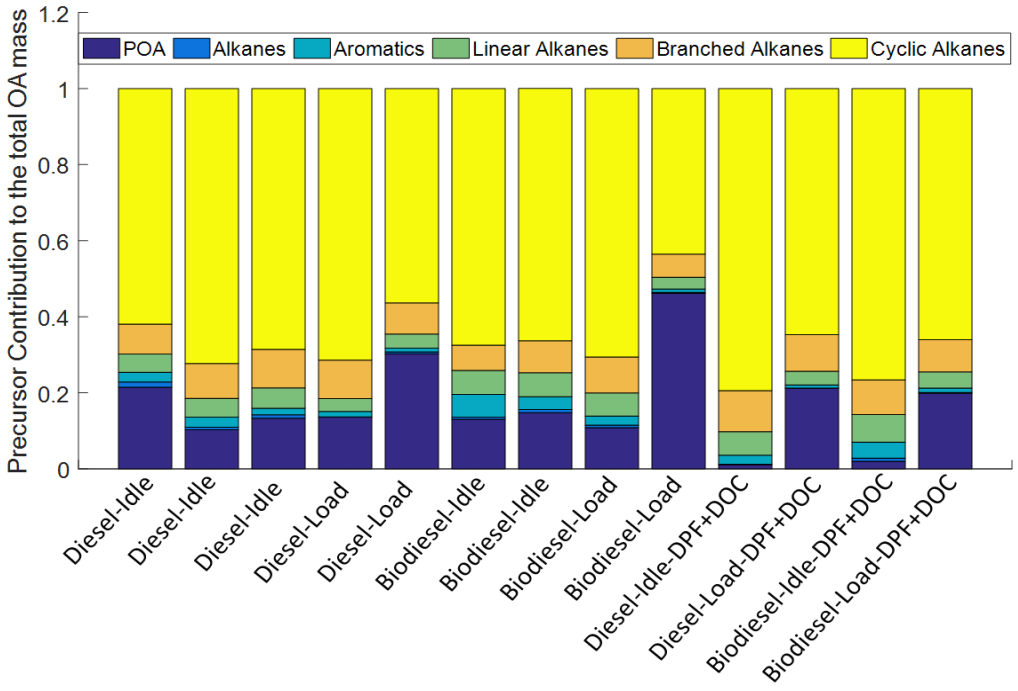

(b)

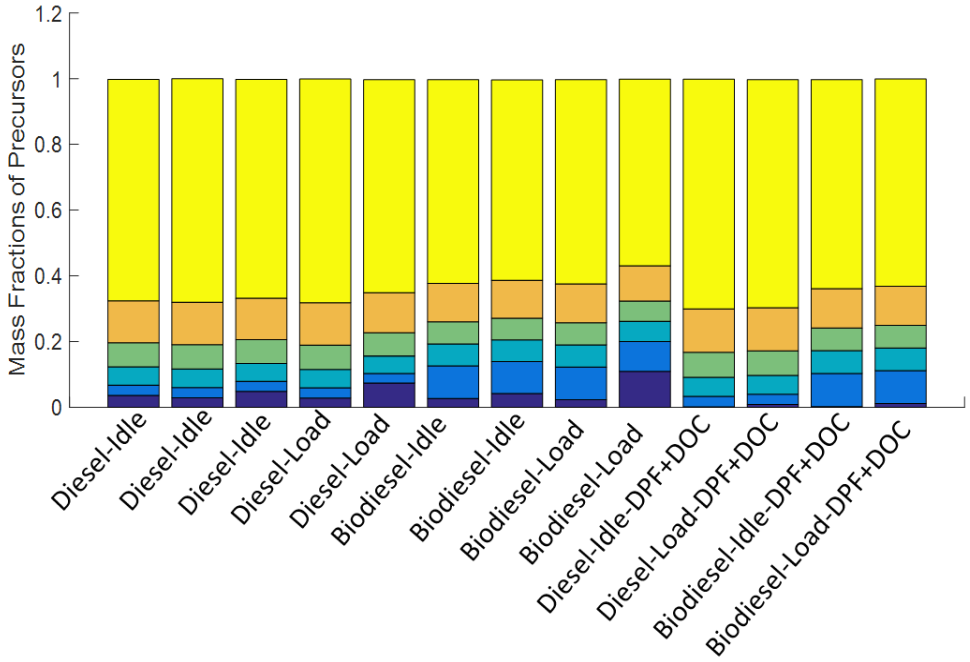

Figure 5: (a) SOM predictions of precursor contribution to the total OA at the highest photochemical age for all the experiments from Table 1. (b) mass fractions of the precursors

Table 6:VBS and SOM model performance for OA mass at 0%,13.6%, and 60% IVOC mass fractions

Aftertreatment	***Model***	***Fractional Bias***			***Fractional Error***			***R^2***		
		0%	13.6%	60%	0%	13.6%	60%	0%	13.6%	60%
None	VBS	-73%	-49%	27%	78%	50%	61%	0.76	0.82	0.84
	SOM	-73%	-33%	43%	78%	61%	55%	0.71	0.91	0.89
DPF+DOC	VBS	-96%	-73%	-17%	104%	85%	36%	0.86	0.98	0.99
	SOM	-127%	-79%	13%	132%	97%	89%	0.87	0.99	0.97

3.4 ELEMENTAL COMPOSITION

The SOM tracks both the carbon and oxygen number of the oxidation products and hence this allowed us to predict the O:C ratio of the OA. In Figure 6, we use scatter plots to compare predictions of the O:C of OA from the SOM model against measurements for all the experiments listed in Table 1 and at all photochemical ages; the O:C measurements were estimated from the aerosol mass spectrometer data collected by Jathar et al. (2017). The model performance for O:C is also captured using statistical metrics of fractional bias, fractional error, and R^2 in Table 7. We note that the O:C of the OA was calculated by combining the measured O:C of the POA with the modeled O:C of the SOA. The model-measurement comparison for the no IVOC case suggests that with very little SOA, the O:C of the OA was dominated by the O:C of the POA and hence the model under-predicted the O:C (fractional bias> -145%and fractional error>147%) and had very little skill. The 13.6% and 60% IVOC cases offered similar model performance (fractional bias>-42% and fractional error>43%) although both cases still under-predicted the OA O:C by about a factor of two. We were also able to compare model predictions of normalized gas-phase species concentrations from the SOM to normalized gas-phase measurements made by Friedman et al. (in preparation), during the same set of experiments, using a chemical ionization mass spectrometer (CIMS). The comparison at the highest photochemical exposure for June 5 is

shown in Figure 7. There are three interesting findings of note: (1) The CIMS measured organic compounds with high O:C ratios (e.g., $C_{12}O_7$), implying mechanisms at play where the reaction chemistry rapidly adds functional groups to the carbon backbone (Ehn et al., 2014). (2) The CIMS was able to measure C_{12+} species, which indicate possible products of IVOC oxidation. (3) The SOM offered a surprisingly reasonable comparison against the CIMS measurements across all carbon-oxygen combinations that span more than four orders of magnitude. Qualitatively, this finding validates the OA evolution tracked through the generalized SOM mechanism. (4) The SOM under-predicted the fractional contribution of high oxygen number species, but slightly over-predicted the fractional contribution of low-oxygen number species. One of the reasons for this discrepancy is that the SOM, in its current representation, does not explicitly model autooxidation-type reactions and cannot rapidly form species that are highly oxygenated. Based on these comparisons with measurements, it is likely that the SOM model, which is currently designed to add a maximum of four oxygen atoms per reaction step, may need to be extended in terms of its statistical scheme to add more oxygens during each reaction step. The SOM-CIMS comparison is preliminary and we intend to explore the implications of this comparison in future work.

Table 7: SOM model performance for O:C predictions at 0%,13.6%, and 60% IVOC mass fractions.

Aftertreatment	***Fractional Bias***			***Fractional Error***			***R^2***		
	0%	***13.6%***	***60%***	***0%***	***13.6%***	***60%***	***0%***	***13.6%***	***60%***
None	-145%	-75%	-62%	147%	77%	69%	0.71	0.73	0.82
DPF+DOC	-42%	-52%	-42%	43%	52%	43%	0.066	0.069	0.01

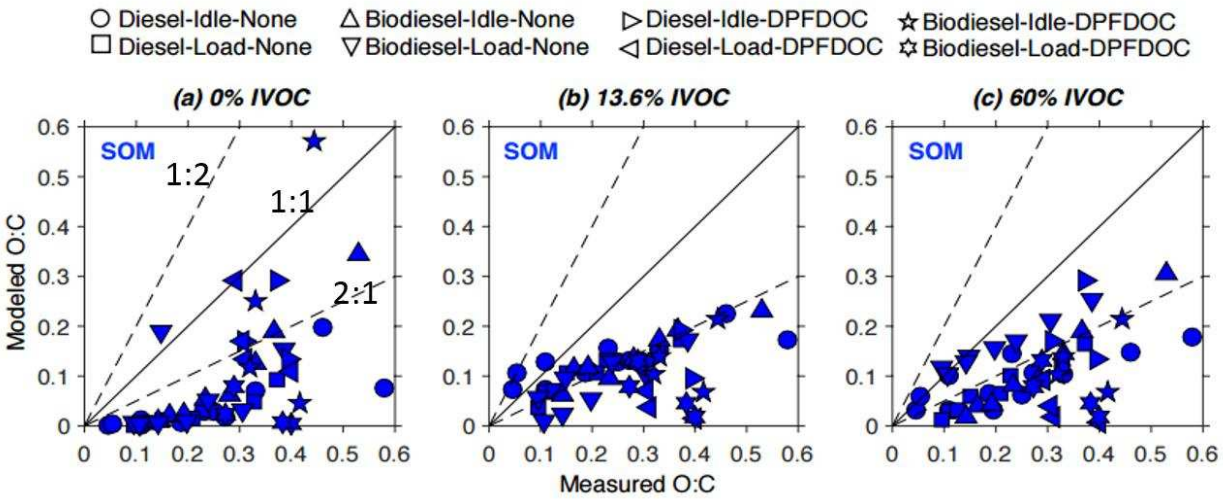

Figure 6: OA O:C predictions from the SOM model assuming 0%, 13.6% and 60% IVOC mass fractions compared to measurements.

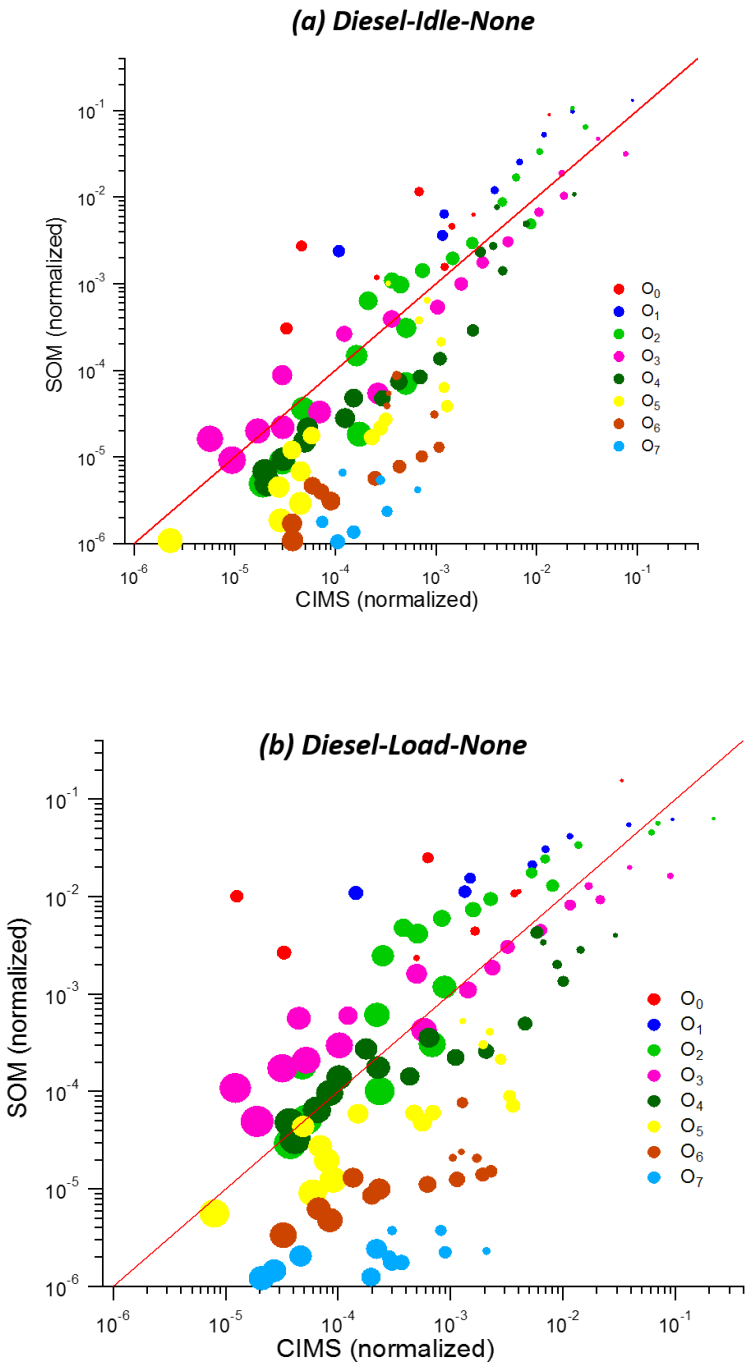

Figure 7: Normalized gas-phase concentrations from the SOM model for the Diesel-Idle-None and Diesel-Load-None experiments compared to normalized gas-phase concentrations measured by the CIMS.

3.5 SENSITIVITY

In this section, we performed sensitivity analyses to examine the influence of key inputs on predictions from both the VBS and SOM models. All the sensitivity simulations were performed on two of the following three experiments: Diesel-Idle-None experiment from June 5, Biodiesel-Idle-None experiment from June 4, Diesel-Idle-DPF+DOC experiment from June 9. When we examined the sensitivity to each model input, we kept all the other inputs the same as those listed in the base set.

3.5.1 IVOC SPECIATION

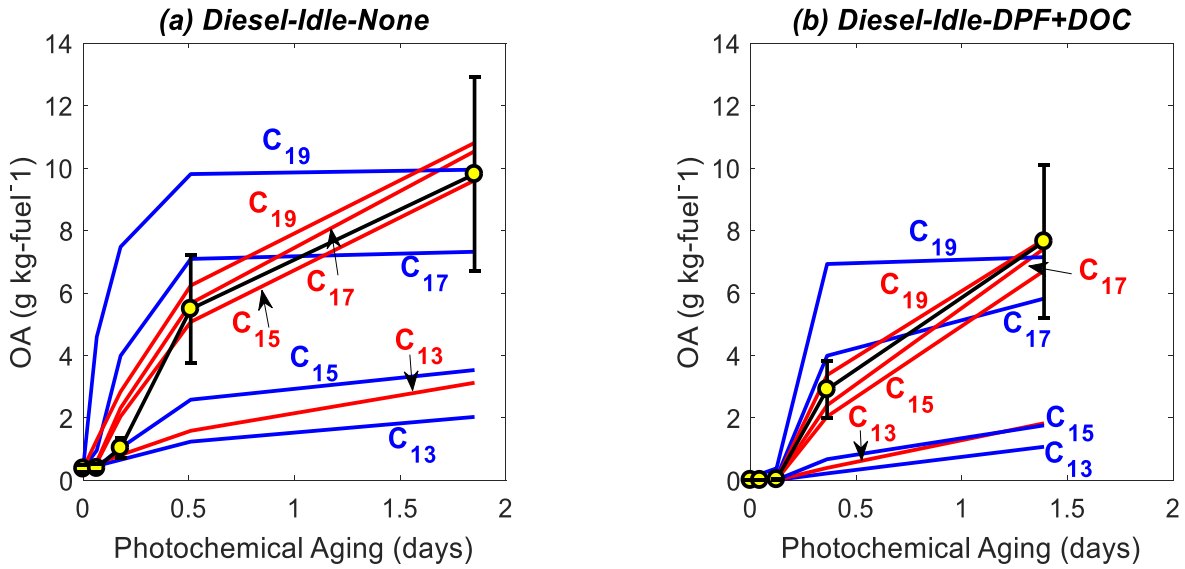

Figure 8: VBS and SOM predictions from using different single surrogates to model SOA formation from IVOCs. Simulations were performed for the (a) Diesel-Idle-None and (b) Diesel-Idle-DPF+DOC experiments.

In Section 3.3, we found that IVOCs were the dominant precursor of SOA production and the model required 40% of the THC emissions to be composed of IVOCs to allow for a good model-measurement comparison. However, the IVOC speciation included 37 unique species, each of

which required a unique surrogate to model the SOA formation from that species. Tracking these many IVOC species in a large-scale model may be intractable and hence we used a strategy previously suggested by Jathar et al. (2014) where we model SOA formation from IVOCs using a single surrogate. We modeled SOA from IVOCs assuming that all the IVOCs together could be modeled as a linear C_{13}, C_{15}, C_{17} *or* C_{19} alkane. Results from these simulations are shown in Figure 8. For the VBS model, the use of a linear C_{15}, C_{17} *and* C_{19} alkane parameterization for IVOCs reproduced the measurements well while for the SOM model, the use of a linear C_{17} alkane parameterization produced good agreement with the measurements. These results indicate that in cases where computationally efficiency is demanded, the SOA formation from IVOCs in diesel exhaust could be modeled using a surrogate linear alkane.

3.5.2 EMISSIONS PROFILE

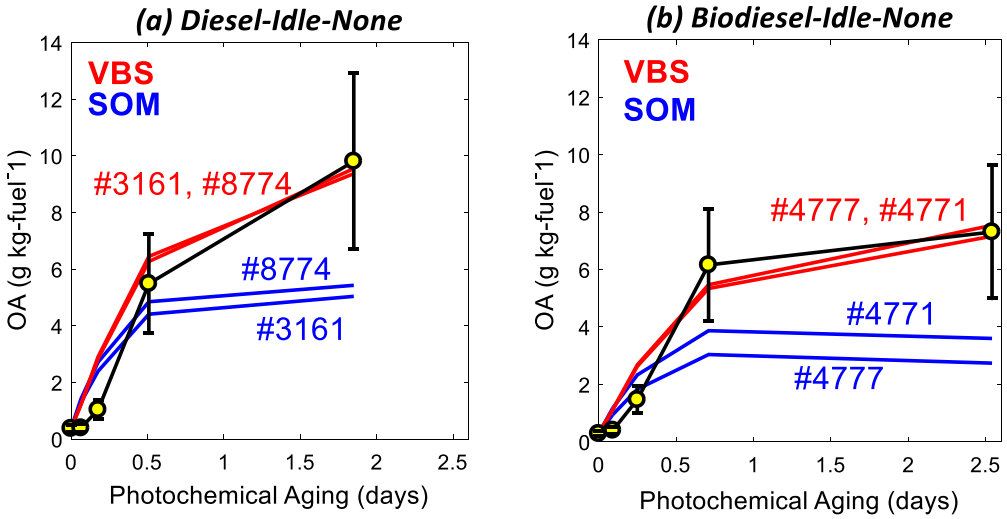

Figure 9: VBS and SOM predictions from using different emission profiles to model SOA formation. Simulations were performed for the (a) Diesel-Idle-None and (b) Biodiesel-Idle-None experiments.

Since there were no direct measurements of the SOA precursors in the study of Jathar et al. (2017), we had to rely on previously published emissions profiles for diesel and biodiesel exhaust to determine initial concentrations of the SOA precursors. Here, we examined the sensitivity of model predictions to Profile #8777 and Profile #4771 for diesel and biodiesel respectively; these profiles are listed in detail in Tables 13 and 14 of the supplementary information. These emissions profiles do not include IVOCs. As there is only a single study so far that has provided a speciation for IVOCs in diesel exhaust (Zhao et al., 2015), we keep the IVOC speciation the same in these simulations. Results from these simulations are captured in Figure 9 where we found that the choice of the emissions profile has very little influence on the OA evolution. This demonstrates that IVOCs, rather than VOCs, play an important role in controlling the SOA formation from diesel exhaust and it is important that future studies work towards understanding the composition of IVOCs.

3.5.3 PARTICLE SIZE DISTRIBUTION

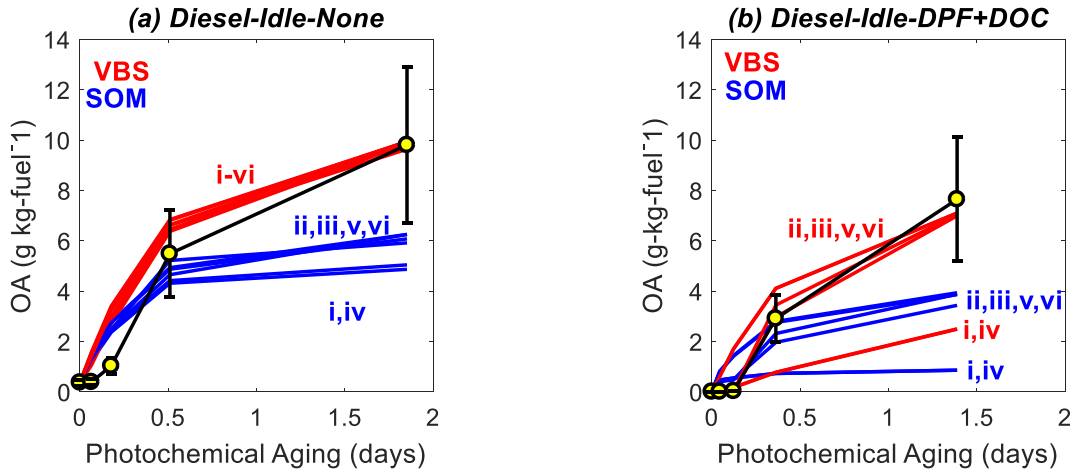

Figure 10 VBS and SOM model predictions from using different particle size distribution inputs. Simulations were performed for the (a) Diesel-Idle-None and (b) Diesel-Idle-DPF+DOC experiments. Legend: (i) surface area mean diameter and measured number concentration at no OH exposure, (ii) surface area mean diameter and measured number concentration at the

highest OH exposure, (iii) surface area mean diameter and measured number concentration at the given photochemical exposure, (iv) number mean diameter and measured number concentration at no OH exposure, (v) number mean diameter and measured number concentration at the highest OH exposure, (vi)average of (i) and (iii)

The particle size distribution inputs, namely the particle diameter and number concentration, control the condensation sink and condensation timescale and given the short residence times in the OFR can control the amount of SOA produced in the OFR. Hence, we investigated the sensitivity of particle size distribution inputs to model predictions of OA. There were two reasons why the particle size distribution inputs specified with our base model ((i) for Diesel-Idle/Load-None experiments and (iii) for Diesel-Idle/Load-DPF+DOC experiments) were not necessarily representative. First, it was unclear how the input particle diameter needed to be calculated given that our model formulation assumed a monodisperse distribution; future work needs to investigate this assumption. And second, in most experiments, Jathar et al. (2017) observed strong nucleation and growth events at the highest photochemical exposure that dramatically increased (by a factor of ~4) the number concentration. These higher concentrations at the high photochemical exposures could possibly have increased the condensation sink to influence the partitioning of SOA. To address uncertainties in the calculation of the initial particle diameter and account for the increased number concentration at high photochemical exposures, we performed five different simulations with each model (VBS and SOM) where we used different particle diameter-number concentration pairs as inputs to the simulation. The five different particle diameter-number concentration inputs were: (i) surface area mean diameter and measured number concentration at no OH exposure, (ii) surface area mean diameter and measured number concentration at the highest OH exposure, (iii) surface area mean diameter and measured number concentration at the given photochemical exposure, (iv) number mean diameter and measured number concentration at no OH exposure, (v) number mean diameter and

measured number concentration at the highest OH exposure, (vi) average of (i) and (iii). Results from these model simulations are shown in Figure 10. We find that the different particle size distribution inputs had very little influence on the VBS model predictions of OA and some influence on the SOM model predictions of OA for the Diesel-Idle-None experiment. The SOM model that used the particle diameter-number concentration pair from no OH exposure produced slightly lower OA estimates (20%) because of a smaller condensation sink. In contrast, for both models we find large differences in the model predictions of OA for the Diesel-Idle-DPF+DOC experiment. The use of the particle diameter-number concentration pair at no OH exposure, where the aftertreatment system significantly reduced number concentrations and hence the available condensation sink, produced much lower OA mass. It appears that the particle size distribution inputs are more important when the condensation sink associated with the initial concentrations are small (>0.00004s^{-1}).

3.5.4 VAPOR WALL LOSSES

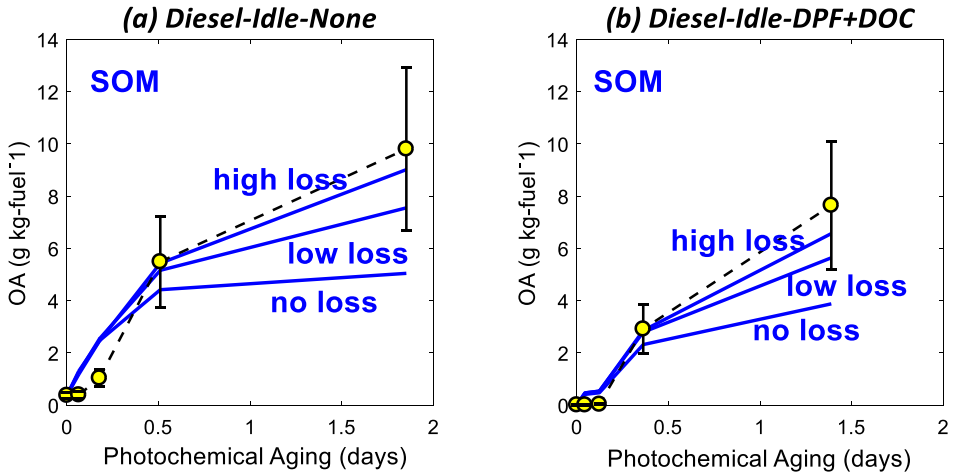

Figure 11 SOM model predictions from using different vapor wall-loss rates. Simulations were performed for the (a) Diesel-Idle-None and (b) Diesel-Idle-DPF+DOC experiments.

Previous research has highlighted the influence vapor wall losses exert on the calculation of SOA mass yields from chamber experiments (Zhang et al., 2014; Krechmer et al., 2015). Cappa et al. (2016), based on the chamber work of Zhang et al. (2014), recently published parameterizations for the SOM model that accounted for vapor wall losses assuming wall loss rates of 1×10^{-4} and 2.5×10^{-4} s^{-1}; these parameters are reproduced in Tables 15 and 16 in the supplementary information. We performed model simulations with the SOM model assuming no wall losses and using the low (1×10^{-4}) and high (2.5×10^{-4}) estimates for vapor wall losses. The results from those simulations are shown in Figure 11. We found that the inclusion of vapor wall losses increased model predicted of OA mass (OA mass assuming high wall loss rates was about 1.8 to 2.4 times higher than those without considering wall losses) and provided the best performance for the high estimate for vapor wall losses. These comparisons further demonstrate that vapor wall losses need to be accounted for in SOA models that are used to interpret chamber and OFR experiments.

3.5.5 MOLECULAR WEIGHT ASSUMPTION

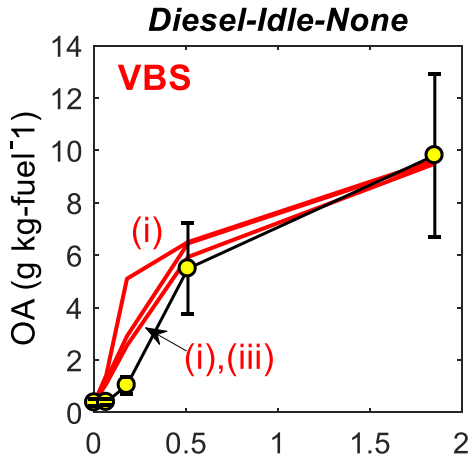

Figure 12: VBS predictions from using different molecular weights for the condensing species. Simulations were performed for the Diesel-Idle-None experiment.

The VBS model does not track the molecular composition of the oxidation products and hence we assumed that all oxidation products had a molecular weight of 300 g mole^{-1}. To investigate the sensitivity on model predictions, we performed simulations with three different molecular weights (i) 100 g mole^{-1} ii) 300 g mole^{-1} and iii) 500 g mole^{-1}. We found that a molecular weight of 100 g mole^{-1} resulted in higher OA mass, especially at lower photochemical ages, since the condensation sink linked to a smaller molecular weight species is larger (see equations in Section 2.3). However, there were few differences in model predictions that used molecular weights of 300 and 500 g mole^{-1}. Since most condensing SOA species are expected to have molecular weights larger than 150 g mole^{-1} (Cappa et al., 2011), we conclude that value used for the molecular weight of the condensing species in the VBS model has little influence on model predictions.

3.5.6 OH VARIATION IN OFR

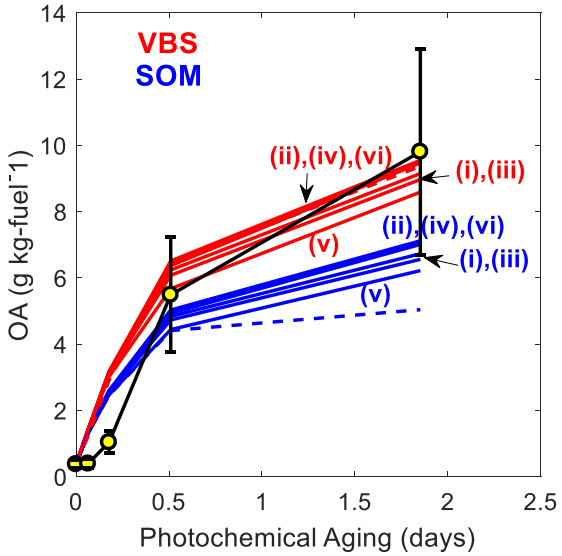

Figure 13: VBS and SOM model predictions of OA as a function of photochemical age by varying the OH concentration. Simulations were performed for: (i)1/4 VOC at 1/3 OH concentration, (ii)1/4 VOC at 2/3 OH concentration, (iii) 1/3 VOC at 1/3 OH concentration, (iv) 1/3 VOC at 2/3 OH concentration, (v)1/2 VOC at 1/3 OH concentration and (vi)1/2 VOC at 2/3 OH, Dashed- Constant OH concentration

In this work, for all the simulations we assumed that the concentration of OH is constant throughout the OFR. Jathar et al.,2017 used one mercury lamp in the OFR that can have impact in the results since the area near the light will have higher exposure compared to the rest of the reactor. To test this, we performed simulations for SOM and VBS by running the models at 1/3 and 2/3 of the OH concentration and we assumed the VOC reacted to be 1/4,1/3 and 1/2 of the overall VOC and did the weighted average to calculate the total OA predicted. Simulations performed were: (i) 1/4 VOC at 1/3 OH concentration, (ii) 1/4 VOC at 2/3 OH concentration, (iii) 1/3 VOC at 1/3 OH concentration, (iv) 1/3 VOC at 2/3 OH concentration, (v) 1/2 VOC at 1/3 OH concentration and (vi) 1/2 VOC at 2/3 OH concentration. For all the simulations, we conserved the OH to be consistent with the calculated OH concentration. Results are plotted in figure (13) in which the dashed lines are default assumption of this work, which is, considering OH concentration constant throughout the OFR. We found that for VBS, the variation did not have much difference compared to the default assumption but in the case of SOM, considering the variation in OH did improve the predictions.

3.5.7 *GAS-PHASE DIFFUSION COEFFICIENT*

The gas-phase diffusion co-efficient for the species used in VBS and SOM were calculated by scaling the diffusion coefficient of CO_2. To study the sensitivity on model predictions, we performed simulations with VBS model by choosing the literature values of gas-phase diffusion coefficients (Tang et al.,2015) for the species in the emission profile and compared to those calculated based on scaling CO_2 (equation 10). Figure (a) shows the comparison of OA predictions as a function of photochemical age for the two different simulations. We found that the model predictions of OA by following the assumption of gas-phase diffusion coefficients of

species by scaling CO_2 value did not have large difference compared to the OA predictions when used literature values for diffusion coefficients. Figure (b) shows the scatter plot of the diffusion coefficients for the few species measured in Tang et al compared to those calculated using equation 10. We can say from the figure (b) that there is no great difference in the diffusion coefficient values based on (i) and (ii) methods.

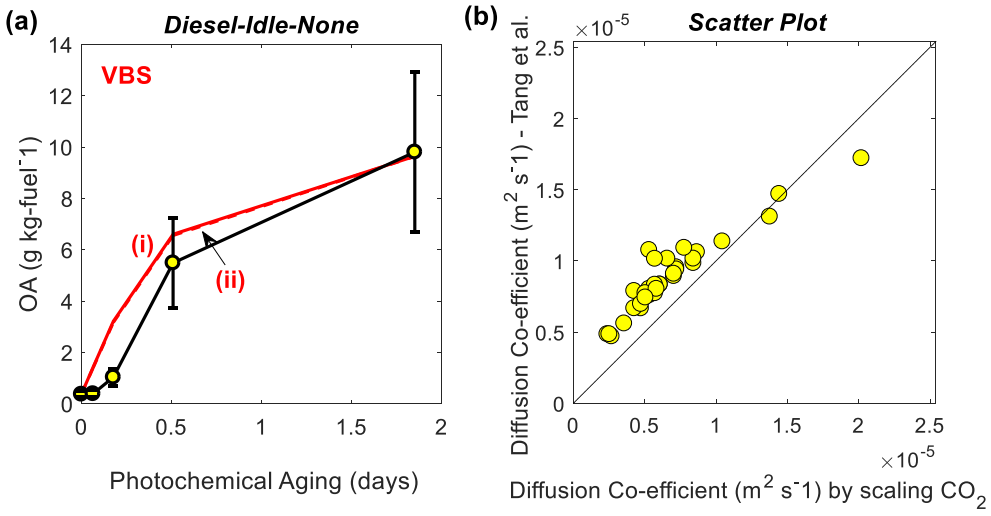

Figure 14: (a) VBS predictions of OA from using different approaches in gas-phase diffusion coefficients as a function of photochemical age. (b) Scatter plot. Simulations were performed for (a): (i) gas-phase diffusion coefficients of species from scaling the diffusion coefficient of CO_2 (solid) and (ii) gas-phase diffusion coefficients for species using literature values (dashed)

3.5.8 YIELDS OF HIGHER ALKANES (C_{17}-C_{22}):

In VBS, since we did not have the product distributions for higher alkanes ($C_{18} – C_{22}$) we considered mass yields of C_{17} for higher alkane numbers for all the simulations of this work. Presto et al., 2010 found that for n-alkanes, addition of 2 carbon atoms shifted the corresponding product distribution by one C* bin or one order of magnitude in C* base. Based on this, we calculated the product distributions of higher alkanes and performed simulations to test the

sensitivity in OA formation from the two approaches. We found that there was no large influence seen in the model predictions following the two approaches.

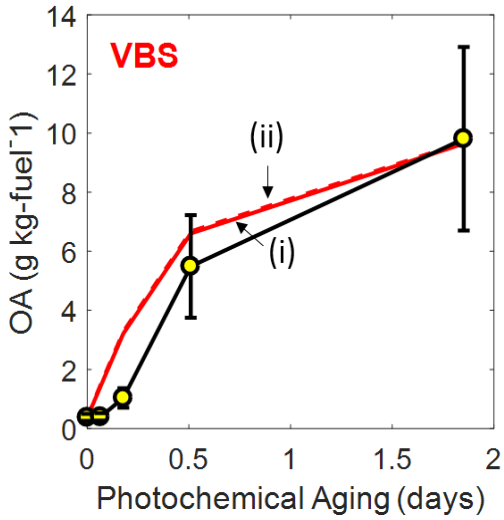

Figure 15: VBS predictions of OA as a function of photochemical age. Simulations performed for: (i) C_{17} product distribution for C_{18} - C_{22} (solid) and (ii) Using the corresponding product distributions for C_{18}-C_{22} alkanes (dashed)

SUMMARY, CONCLUSIONS AND FUTURE WORK

Recently, Jathar et al. (2017) performed experiments using the oxidation flow reactor (OFR) to measure the photochemical production of secondary organic aerosol (SOA) from diesel exhaust under varying engine loads, fuel types, and emissions control systems. These data present an opportunity to test SOA models and project their relevance for the atmosphere. However, most traditional treatments of SOA models do not include (i) emissions and a detailed speciation of intermediate volatility organic compounds (IVOCs) that have been recognized to be important SOA precursors and (ii) kinetic gas/particle partitioning, which is likely to be relevant for processes inside an OFR. In this work, we developed and applied two different SOA model frameworks (VBS and SOM) to simulate the photochemical production of SOA in an OFR from diesel exhaust and evaluated those model frameworks using the data from Jathar et al. (2017). The volatility basis set (VBS) model is a parameterized model that allows for a volatility-based representation of OA while the statistical oxidation model (SOM) is a semi-explicit parameterized model that uses a carbon-oxygen grid to track OA species. Both simulate the coupled chemistry, thermodynamic properties, and gas/particle partitioning of OA and in this work accounted for: (i) semi-volatile and reactive emissions of primary organic aerosol (POA), (ii) NO_x-dependent SOA production from IVOCs and VOCs, (iii) multi-generational aging, and (iv) kinetic gas/particle partitioning.

On including IVOCs as SOA precursors, both the VBS and SOM models were able to reasonably predict the OA evolution reported by Jathar et al. (2017) across different engine loads, fuel types, and emissions control systems. Model predictions suggested that at least 40% of the unburned

hydrocarbon emissions were IVOCs and that these IVOCs (regardless of the emissions profiles used to determine non-IVOC emissions) accounted for most (>90%) of the SOA formed from diesel exhaust. These findings are consistent with those from prior work performed on chamber experiments (Jathar et al., 2014). Simulations performed using single surrogates to model SOA formation from IVOCs suggested that the complex mixture of IVOCs in diesel exhaust could be well represented using a linear C_{15} or C_{17} alkane. These offer a computationally-efficient strategy to model SOA formation from IVOCs in large-scale three-dimensional models.

While the inclusion of IVOCs allowed for good model-measurement comparison on OA mass, model predictions were unable to accurately predict the elemental composition of OA. The SOM model tracks the carbon and oxygen numbers of the oxidation products and hence model predictions were used to calculate atomic O:C ratios for OA, which were then compared to measurements. The current formulation of the SOM under-predicted the O:C ratio of the OA by a factor of two. Comparisons of model predictions in the gas-phase to those measured using a chemical ionization mass spectrometer (CIMS) suggested that the SOM may need to be modified to include mechanisms for rapid addition of oxygen-based functional groups to the carbon backbone to improve model performance.

Model predictions suggested that kinetic gas/particle partitioning and inclusion of vapor wall-losses was necessary to model OFR SOA data. Specifically, the mass accommodation coefficient could not be much smaller than 0.1 and the vapor wall-loss rates needed to be at least 2.5×10^{-4} s^{-1} to reproduce the observed evolution of OA. We also discovered that the instantaneous or

equilibrium gas/particle partitioning assumption led to over-predictions of the condensation and formation of SOA and may not be suitable to model OFR data.

As OFRs are increasingly used to study SOA formation and evolution in laboratory and field environments, there is a need to develop models that can be used to interpret the OFR data. This work is one example of the model development and application relevant to the use of OFRs. There are several instances where the model development was insufficient and will likely be addressed in future work. For example, the model could benefit from the use of a polydisperse size distribution, explicit treatment of nucleation, and the inclusion of Kelvin effects to improve predictions of the size distribution evolution. Confidence in the models developed here could also be built by testing the models against other OFR data (Palm et al., 2015). Finally, simple parameterizations could be developed based on this model to represent SOA formation in large-scale models where it may not be possible to track the hundreds of precursor species dealt in this work.

REFERENCES

1. Pachauri, R. K.; Allen, M. R.; Barros, V. R.; Broome, J.; Cramer, W.; Christ, R.; Church, J. A.; Clarke, L.; Dahe, Q.; Dasgupta, P.; Dubash, N. K.; Edenhofer, O.; Elgizouli, I.; Field, C. B.; Forster, P.; Friedlingstein, P.; Fuglestvedt, J.; Gomez-Echeverri, L.; Hallegatte, S.; Hegerl, G.; Howden, M.; Jiang, K.; Jimenez Cisneroz, B.; Kattsov, V.; Lee, H.; Mach, K. J.; Marotzke, J.; Mastrandrea, M. D.; Meyer, L.; Minx, J.; Mulugetta, Y.; O'Brien, K.; Oppenheimer, M.; Pereira, J. J.; Pichs-Madruga, R.; Plattner, G. K.; Pörtner, H.-O.; Power, S. B.; Preston, B.; Ravindranath, N. H.; Reisinger, A.; Riahi, K.; Rusticucci, M.; Scholes, R.; Seyboth, K.; Sokona, Y.; Stavins, R.; Stocker, T. F.; Tschakert, P.; van Vuuren, D.; van Ypserle, J. P., *Climate Change 2014: Synthesis Report. Contribution of Working Groups I, II and III to the Fifth Assessment Report of the Intergovernmental Panel on Climate Change*. IPCC: Geneva, Switzerland, 2014; p 151.
2. Anderson, J. O.; Thundiyil, J. G.; Stolbach, A., Clearing the air: a review of the effects of particulate matter air pollution on human health. *Journal of Medical Toxicology* **2012,** *8*, (2), 166-175.
3. Jacobson, M. C., Hansson, H. C., Noone, K. J., & Charlson, R. J. (2000). Organic atmospheric aerosols: Review and state of the science. *Reviews of Geophysics*, *38*(2), 267-294.
4. Bond, T.C., Doherty, S.J., Fahey, D.W., Forster, P.M., Berntsen, T., DeAngelo, B.J., Flanner, M.G., Ghan, S., Kärcher, B., Koch, D. and Kinne, S., 2013. Bounding the role of black carbon in the climate system: A scientific assessment. *Journal of Geophysical Research: Atmospheres*, *118*(11), pp.5380-5552.
5. Robinson, Allen L., Neil M. Donahue, Manish K. Shrivastava, Emily A. Weitkamp, Amy M. Sage, Andrew P. Grieshop, Timothy E. Lane, Jeffrey R. Pierce, and Spyros N. Pandis. "Rethinking organic aerosols: Semivolatile emissions and photochemical aging." *Science* 315, no. 5816 (2007): 1259-1262.
6. Goldstein, A. H., & Galbally, I. E. (2007). Known and unexplored organic constituents in the earth's atmosphere. *Environmental Science & Technology*, *41*(5), 1514-1521.
7. Jathar, S.H., Gordon, T.D., Hennigan, C.J., Pye, H.O., Pouliot, G., Adams, P.J., Donahue, N.M. and Robinson, A.L., 2014. Unspeciated organic emissions from combustion sources and their influence on the secondary organic aerosol budget in the United States. *Proceedings of the National Academy of Sciences*, *111*(29), pp.10473-10478.
8. Fuzzi, S., Baltensperger, U., Carslaw, K., Decesari, S., Denier Van Der Gon, H., Facchini, M.C., Fowler, D., Koren, I., Langford, B., Lohmann, U. and Nemitz, E., 2015. Particulate matter, air quality and climate: lessons learned and future needs. *Atmospheric Chemistry and Physics*, *15*(14), pp.8217-8299.
9. Carlton, A.G., Bhave, P.V., Napelenok, S.L., Edney, E.O., Sarwar, G., Pinder, R.W., Pouliot, G.A. and Houyoux, M., 2010. Model representation of secondary organic aerosol in CMAQv4. 7. *Environmental science & technology*, *44*(22), pp.8553-8560.
10. Chirico, R., DeCarlo, P.F., Heringa, M.F., Tritscher, T., Richter, R., Prévôt, A.S.H., Dommen, J., Weingartner, E., Wehrle, G., Gysel, M. and Laborde, M., 2010. Impact of aftertreatment devices on primary emissions and secondary organic aerosol formation potential from in-use diesel vehicles: results from smog chamber experiments. *Atmospheric Chemistry and Physics*, *10*(23), pp.11545-11563.

11. Gordon, T.D., Presto, A.A., Nguyen, N.T., Robertson, W.H., Na, K., Sahay, K.N., Zhang, M., Maddox, C., Rieger, P., Chattopadhyay, S. and Maldonado, H., 2014. Secondary organic aerosol production from diesel vehicle exhaust: impact of aftertreatment, fuel chemistry and driving cycle. *Atmospheric Chemistry and Physics*, *14*(9), pp.4643-4659.
12. Tkacik, D.S., Lambe, A.T., Jathar, S., Li, X., Presto, A.A., Zhao, Y., Blake, D., Meinardi, S., Jayne, J.T., Croteau, P.L. and Robinson, A.L., 2014. Secondary organic aerosol formation from in-use motor vehicle emissions using a potential aerosol mass reactor. *Environmental science & technology*, *48*(19), pp.11235-11242.
13. Jathar, Shantanu H., Beth Friedman, Abril A. Galang, Michael F. Link, Patrick Brophy, John Volckens, Sailaja Eluri, and Delphine K. Farmer. "Linking Load, Fuel and Emission Controls to Photochemical Production of Secondary Organic Aerosol from a Diesel Engine." *Environmental Science & Technology* (2017).
14. Lambe, A. T.; Ahern, A. T.; Williams, L. R.; Slowik, J. G.; Wong, J. P. S.; Abbatt, J. P. D.; Brune, W. H.; Ng, N. L.; Wright, J. P.; Croasdale, D. R., Characterization of aerosol photooxidation flow reactors: heterogeneous oxidation, secondary organic aerosol formation and cloud condensation nuclei activity measurements. *Atmospheric Measurement Techniques* **2011,** *4*, (3), 445-461.
15. Palm, B.B., Campuzano-Jost, P., Ortega, A.M., Day, D.A., Kaser, L., Jud, W., Karl, T., Hansel, A., Hunter, J.F., Cross, E.S. and Kroll, J.H., 2016. In situ secondary organic aerosol formation from ambient pine forest air using an oxidation flow reactor. *Atmospheric Chemistry and Physics*, *16*(5), pp.2943-2970.
16. Lambe, A.T., Onasch, T.B., Croasdale, D.R., Wright, J.P., Martin, A.T., Franklin, J.P., Massoli, P., Kroll, J.H., Canagaratna, M.R., Brune, W.H. and Worsnop, D.R., 2012. Transitions from functionalization to fragmentation reactions of laboratory secondary organic aerosol (SOA) generated from the OH oxidation of alkane precursors. *Environmental science & technology*, *46*(10), pp.5430-5437.
17. Zhang, X., Cappa, C. D., Jathar, S. H., McVay, R. C., Ensberg, J. J., Kleeman, M. J., & Seinfeld, J. H. (2014). Influence of vapor wall loss in laboratory chambers on yields of secondary organic aerosol. *Proceedings of the National Academy of Sciences*, *111*(16), 5802-5807.
18. Ortega, A. M.; Hayes, P. L.; Peng, Z.; Palm, B. B.; Hu, W.; Day, D. A.; Li, R.; Cubison, M. J.; Brune, W. H.; Graus, M., Real-time measurements of secondary organic aerosol formation and aging from ambient air in an oxidation flow reactor in the Los Angeles area. *Atmospheric Chemistry and Physics* **2016,** *16*, (11), 7411-7433
19. Odum, J. R., Hoffmann, T., Bowman, F., Collins, D., Flagan, R. C., & Seinfeld, J. H. (1996). Gas/particle partitioning and secondary organic aerosol yields. *Environmental Science & Technology*, *30*(8), 2580-2585.
20. Donahue, N. M., Robinson, A. L., Stanier, C. O., & Pandis, S. N. (2006). Coupled partitioning, dilution, and chemical aging of semivolatile organics. *Environmental Science & Technology*, *40*(8), 2635-2643.
21. Pankow, J. F. (1994). An absorption model of gas/particle partitioning of organic compounds in the atmosphere. *Atmospheric Environment*, *28*(2), 185-188.
22. Ng, N. L., Kroll, J. H., Chan, A. W. H., Chhabra, P. S., Flagan, R. C., & Seinfeld, J. H. (2007). Secondary organic aerosol formation from m-xylene, toluene, and benzene. *Atmospheric Chemistry and Physics*, *7*(14), 3909-3922.

23. Chhabra, P. S., Flagan, R. C., & Seinfeld, J. H. (2010). Elemental analysis of chamber organic aerosol using an aerodyne high-resolution aerosol mass spectrometer. *Atmospheric Chemistry and Physics*, *10*(9), 4111-4131.
24. Dzepina, K., Volkamer, R.M., Madronich, S., Tulet, P., Ulbrich, I.M., Zhang, Q., Cappa, C.D., Ziemann, P.J. and Jimenez, J.L., 2009. Evaluation of recently-proposed secondary organic aerosol models for a case study in Mexico City. *Atmospheric Chemistry and Physics*, *9*(15), pp.5681-5709.
25. Murphy, B. N., & Pandis, S. N. (2009). Simulating the formation of semivolatile primary and secondary organic aerosol in a regional chemical transport model. *Environmental science & technology*, *43*(13), 4722-4728.
26. Tsimpidi, A.P., Karydis, V.A., Zavala, M., Lei, W., Molina, L., Ulbrich, I.M., Jimenez, J.L. and Pandis, S.N., 2010. Evaluation of the volatility basis-set approach for the simulation of organic aerosol formation in the Mexico City metropolitan area. *Atmospheric Chemistry and Physics*, *10*(2), pp.525-546.
27. Jathar, S. H., Farina, S. C., Robinson, A. L., & Adams, P. J. (2011). The influence of semi-volatile and reactive primary emissions on the abundance and properties of global organic aerosol. *Atmospheric Chemistry and Physics*, *11*(15), 7727-7746.
28. Konovalov, I. B. (2015). Interactive comment on "The role of semi-volatile organic compounds in the mesoscale evolution of biomass burning aerosol: a modelling case study of the 2010 mega-fire event in Russia" by IB Konovalov et al.
29. Pye, H. O., & Seinfeld, J. H. (2010). A global perspective on aerosol from low-volatility organic compounds. *Atmospheric Chemistry and Physics*, *10*(9), 4377-4401.
30. Zhao, Y., Nguyen, N. T., Presto, A. A., Hennigan, C. J., May, A. A., & Robinson, A. L. (2015). Intermediate volatility organic compound emissions from on-road diesel vehicles: chemical composition, emission factors, and estimated secondary organic aerosol production. *Environmental science & technology*, *49*(19), 11516-11526.
31. Cappa, C. D., & Wilson, K. R. (2012). Multi-generation gas-phase oxidation, equilibrium partitioning, and the formation and evolution of secondary organic aerosol. *Atmospheric Chemistry and Physics*, *12*(20), 9505-9528.
32. Donahue, N. M., Epstein, S. A., Pandis, S. N., & Robinson, A. L. (2011). A two-dimensional volatility basis set: 1. organic-aerosol mixing thermodynamics. *Atmospheric Chemistry and Physics*, *11*(7), 3303-3318.
33. Pankow, J. F., & Barsanti, K. C. (2009). The carbon number-polarity grid: A means to manage the complexity of the mix of organic compounds when modeling atmospheric organic particulate matter. *Atmospheric Environment*, *43*(17), 2829-2835.
34. Chacon-Madrid, H. J., & Donahue, N. M. (2011). Fragmentation vs. functionalization: chemical aging and organic aerosol formation. *Atmospheric Chemistry and Physics*, *11*(20), 10553-10563.
35. Woody, Matthew C., Kirk R. Baker, Patrick L. Hayes, Jose L. Jimenez, Bonyoung Koo, and Havala OT Pye. "Understanding sources of organic aerosol during CalNex-2010 using the CMAQ-VBS." *Atmospheric Chemistry and Physics* 16, no. 6 (2016): 4081-4100.
36. Meng, Zhaoyue, and John H. Seinfeld. "Time scales to achieve atmospheric gas-aerosol equilibrium for volatile species." *Atmospheric Environment* 30, no. 16 (1996): 2889-2900.
37. Zhang, Xiaolu, Jiumeng Liu, Eric T. Parker, Patrick L. Hayes, Jose L. Jimenez, Joost A. Gouw, James H. Flynn, Nicole Grossberg, Barry L. Lefer, and Rodney J. Weber. "On the gas-particle partitioning of soluble organic aerosol in two urban atmospheres with contrasting

emissions: 1. Bulk water-soluble organic carbon." *Journal of Geophysical Research: Atmospheres* 117, no. D21 (2012).
38. Ehn, M., Thornton, J.A., Kleist, E., Sipilä, M., Junninen, H., Pullinen, I., Springer, M., Rubach, F., Tillmann, R., Lee, B. and Lopez-Hilfiker, F., 2014. A large source of low-volatility secondary organic aerosol. *Nature*, *506*(7489), pp.476-479.
39. May, Andrew A., Albert A. Presto, Christopher J. Hennigan, Ngoc T. Nguyen, Timothy D. Gordon, and Allen L. Robinson. "Gas-particle partitioning of primary organic aerosol emissions:(1) Gasoline vehicle exhaust." *Atmospheric Environment* 77 (2013): 128-139.
40. May, Andrew A., Ezra JT Levin, Christopher J. Hennigan, Ilona Riipinen, Taehyoung Lee, Jeffrey L. Collett, Jose L. Jimenez, Sonia M. Kreidenweis, and Allen L. Robinson. "Gas-particle partitioning of primary organic aerosol emissions: 3. Biomass burning." *Journal of Geophysical Research: Atmospheres* 118, no. 19 (2013).
41. Presto, Albert A., Marissa A. Miracolo, Neil M. Donahue, and Allen L. Robinson. "Secondary organic aerosol formation from high-NO x photo-oxidation of low volatility precursors: n-alkanes." *Environmental science & technology* 44, no. 6 (2010): 2029-2034.
42. Presto, Albert A., Ngoc T. Nguyen, Manish Ranjan, Aaron J. Reeder, Eric M. Lipsky, Christopher J. Hennigan, Marissa A. Miracolo, Daniel D. Riemer, and Allen L. Robinson. "Fine particle and organic vapor emissions from staged tests of an in-use aircraft engine." *Atmospheric environment* 45, no. 21 (2011): 3603-3612.
43. Gordon, T. D., A. A. Presto, A. A. May, N. T. Nguyen, E. M. Lipsky, N. M. Donahue, A. Gutierrez et al. "Secondary organic aerosol formation exceeds primary particulate matter emissions for light-duty gasoline vehicles." *Atmospheric Chemistry and Physics* 14, no. 9 (2014): 4661-4678.
44. Krechmer, Jordan E., Matthew M. Coggon, Paola Massoli, Tran B. Nguyen, John D. Crounse, Weiwei Hu, Douglas A. Day et al. "Formation of low volatility organic compounds and secondary organic aerosol from isoprene hydroxyhydroperoxide low-NO oxidation." *Environmental science & technology* 49, no. 17 (2015): 10330-10339.
45. EPA, 2016
46. Tang, M. J., Shiraiwa, M., Pöschl, U., Cox, R. A., & Kalberer, M. (2015). Compilation and evaluation of gas phase diffusion coefficients of reactive trace gases in the atmosphere: Volume 2. Diffusivities of organic compounds, pressure-normalised mean free paths, and average Knudsen numbers for gas uptake calculations. *Atmospheric Chemistry and Physics*, *15*(10), 5585-5598.

APPENDIX

Table 8:Estimated volatility-resolved POA (POC particle) and POC vapor concentrations in µg m-3 used as inputs in the VBS model.

Load-Fuel-Aftertreatment Experiment		***C* (µg m^{-3})***							
		10^{-1}	***10^{0}***	***10^{1}***	***10^{2}***	***10^{3}***	***10^{4}***	***10^{5}***	***10^{6}***
Idle-Diesel-None	POA	1.13	9.45	13.99	8.70	2.27	1.13	0.38	0.38
	POC vapor	0.66	5.52	8.16	5.07	1.32	0.66	0.22	0.22
	POA	1.05	8.71	12.89	8.01	2.09	1.05	0.35	0.35
	Vapor	0.64	5.29	7.83	4.87	1.27	0.64	0.21	0.21
	POA	2.55	21.25	31.45	19.55	5.10	2.55	0.85	0.85
	Vapor	1.00	8.32	12.31	7.65	2.00	1.00	0.33	0.33
Idle-Biodiesel-None	POA	0.66	5.54	8.20	5.09	1.33	0.66	0.22	0.22
	Vapor	0.51	4.23	6.26	3.89	1.01	0.51	0.17	0.17
	POA	2.07	17.24	25.51	15.86	4.14	2.07	0.69	0.69
	Vapor	0.90	7.48	11.07	6.88	1.79	0.90	0.30	0.30
Load-Diesel-None	POA	0.56	4.63	6.85	4.26	1.11	0.56	0.19	0.19
	Vapor	0.46	3.87	5.73	3.56	0.93	0.46	0.15	0.15
	POA	1.12	9.33	13.80	8.58	2.24	1.12	0.37	0.37
	Vapor	0.66	5.48	8.11	5.04	1.31	0.66	0.22	0.22
Load-Biodiesel-None	POA	0.86	7.17	10.62	6.60	1.72	0.86	0.29	0.29
	Vapor	0.58	4.80	7.11	4.42	1.15	0.58	0.19	0.19
	POA	1.37	11.41	16.89	10.50	2.74	1.37	0.46	0.46
	Vapor	0.73	6.07	8.98	5.58	1.46	0.73	0.24	0.24
Idle-Diesel-DPF+DOC	POA	0.04	0.37	0.55	0.34	0.09	0.04	0.01	0.01
	Vapor	0.15	1.25	1.86	1.15	0.30	0.15	0.05	0.05
Load-Diesel-DPF+DOC	POA	0.05	0.41	0.61	0.38	0.10	0.05	0.02	0.02
	Vapor	0.16	1.30	1.93	1.20	0.31	0.16	0.05	0.05
Idle-Biodiesel-DPF+DOC	POA	0.08	0.65	0.96	0.60	0.16	0.08	0.03	0.03
	Vapor	0.19	1.57	2.33	1.45	0.38	0.19	0.06	0.06
Load-Biodiesel-DPF+DOC	POA	0.06	0.53	0.78	0.49	0.13	0.06	0.02	0.02
	Vapor	0.17	1.44	2.14	1.33	0.35	0.17	0.06	0.06

Table 9:Estimated carbon number-resolved POA (POC particle) and POC vapor concentrations in µg m-3 used as inputs in the SOM model

Load-Fuel-Aftert		***Carbon Number***												
		<16	***16***	***17***	***18***	***19***	***20***	***21***	***22***	***23***	***24***	***25***	***26***	***>26***

reatment Experiment														
Idle-Diesel-None	POA	0.13	0.005	2.20	1.61	2.07	3.57	5.53	6.84	6.71	5.17	2.93	0.99	0.05
	POC Vapor	0.07	0.00	1.28	0.94	1.20	2.07	3.20	3.96	3.89	3.00	1.70	0.57	0.03
	POA	0.12	0.01	2.03	1.49	1.91	3.29	5.09	6.30	6.19	4.77	2.70	0.91	0.05
	POC Vapor	0.07	0.00	1.23	0.90	1.15	1.99	3.08	3.81	3.74	2.88	1.63	0.55	0.03
	POA	0.29	0.01	4.95	3.63	4.66	8.02	12.43	15.34	15.09	11.63	6.59	2.23	0.11
	POC Vapor	0.11	0.01	1.91	1.40	1.80	3.09	4.79	5.93	5.82	4.49	2.54	0.86	0.04
Idle-Biodiesel-None	POA	0.07	0.00	1.29	0.95	1.21	2.09	3.24	4.01	3.93	3.03	1.72	0.58	0.03
	POC Vapor	0.06	0.00	0.99	0.72	0.93	1.59	2.47	3.06	3.00	2.31	1.31	0.44	0.02
	POA	0.23	0.01	4.02	2.94	3.78	6.50	10.08	12.47	12.24	9.43	5.34	1.81	0.09
	POC Vapor	0.10	0.00	1.72	1.26	1.62	2.78	4.31	5.34	5.24	4.04	2.29	0.77	0.04
Load-Diesel-None	POA	0.06	0.00	1.08	0.79	1.02	1.75	2.71	3.35	3.29	2.53	1.44	0.49	0.02
	POC Vapor	0.05	0.00	0.90	0.66	0.85	1.46	2.27	2.81	2.76	2.12	1.20	0.41	0.02
	POA	0.13	0.01	2.17	1.59	2.05	3.52	5.46	6.75	6.62	5.11	2.89	0.98	0.05
	POC Vapor	0.07	0.00	1.27	0.93	1.19	2.05	3.18	3.94	3.86	2.98	1.69	0.57	0.03
Load-Biodiesel-None	POA	0.10	0.00	1.67	1.23	1.57	2.71	4.20	5.19	5.09	3.93	2.22	0.75	0.04
	POC Vapor	0.06	0.00	1.12	0.82	1.05	1.81	2.80	3.46	3.40	2.62	1.48	0.50	0.03
	POA	0.15	0.01	2.66	1.95	2.50	4.31	6.68	8.26	8.10	6.25	3.54	1.20	0.06
	POC Vapor	0.08	0.00	1.40	1.03	1.32	2.27	3.52	4.35	4.27	3.29	1.86	0.63	0.03
Idle-Diesel-DPF+DOC	POA	0.01	0.00	0.09	0.06	0.08	0.14	0.22	0.27	0.27	0.20	0.12	0.04	0.00
	POC Vapor	0.02	0.00	0.30	0.22	0.29	0.49	0.76	0.94	0.93	0.71	0.40	0.14	0.01
Load-Diesel-DPF+DOC	POA	0.01	0.00	0.10	0.07	0.09	0.16	0.24	0.30	0.29	0.22	0.13	0.04	0.00
	POC Vapor	0.02	0.00	0.32	0.23	0.30	0.51	0.79	0.98	0.96	0.74	0.42	0.14	0.01
Idle-Biodiesel-DPF+DOC	POA	0.01	0.00	0.15	0.11	0.14	0.24	0.38	0.47	0.46	0.35	0.20	0.07	0.00
	POC Vapor	0.02	0.00	0.38	0.28	0.35	0.61	0.95	1.17	1.15	0.89	0.50	0.17	0.01
Load-Biodiesel-DPF+DOC	POA	0.01	0.00	0.12	0.09	0.12	0.20	0.31	0.38	0.38	0.29	0.16	0.06	0.00
	POC Vapor	0.02	0.00	0.35	0.25	0.33	0.56	0.87	1.08	1.06	0.82	0.46	0.16	0.01

Table 10:Profile numbers form EPA SPECIATE version 4.3 commonly used to speciate THC emissions in diesel exhaust.

EPA Profile Number	***Type***
3161	Farm Equipment- Diesel
8774	Heavy duty diesel exhaust
4777	Biodiesel Exhaust-Light Duty
4771	Biodiesel Exhaust- Light Duty

Table 11:VOC emissions profile #3161 -Diesel Exhaust-Farm Equipment

Species Name	***kOH (cm^3 $molecules^{-1}s^{-1}$)***	***Mass Percent***
(1-methylpropyl) benzene	8.5e-12	0.023
(2-methylpropyl) benzene	8.71e-12	0.060
1,2,3-trimethylbenzene	3.27e-11	0.056
1,2,4-trimethylbenzene	3.25e-11	0.246
1,2-diethylbenzene	8.11e-12	0.042
1,2-propadiene	9.82e-12	0.218
1,3,5-trimethylbenzene	5.67e-11	0.088
1,3-butadiene	6.66e-11	0.088
1-butene	3.14e-11	0.311
1-methyl-2-ethylbenzene	7.44e-12	0.065
1-methyl-3-ethylbenzene	1.39e-11	0.116
1-pentene	3.14e-11	0.148
2,2,4-trimethylpentane	3.34e-12	0.139
2,2-dimethylbutane	2.23e-12	0.028
2,3,4-trimethylpentane	6.6e-12	0.009
2,3-dimethyl-1-butene	5.38e-11	0.014
2,3-dimethylhexane	8.55e-12	0.005
2,3-dimethylpentane	7.14e-12	0.032
2,4-dimethylhexane	8.55e-12	0.019
2,4-dimethylpentane	4.77e-12	0.009
2-methylheptane	8.28e-12	0.028
2-methylhexane	6.86e-12	0.056
2-methylpentane	5.2e-12	0.181
3,3-dimethyl-1-butene	2.8e-11	1.308
3-ethylhexane	8.97e-12	0.028
3-methylhexane	7.15e-12	0.162
3-methylpentane	5.2e-12	0.056
acetaldehyde	1.5e-11	3.409
acetone	1.7e-13	3.483
acetylene	8.15e-13	1.971
alkene ketone	1.7e-13	0.812
b-methylstyrene	3.12e-11	0.023

benzaldehyde	1.2e-11	0.325
benzene	1.22e-12	0.928
butyraldehyde	2.4e-11	0.867
c10 aromatics	2.3e-11	0.037
c5 aldehyde	2.88e-11	0.051
c6 aldehydes	2.88e-11	1.763
c9 aromatics	2.31e-11	0.232
cis-2-butene	5.64e-11	0.042
cis-2-pentene	6.5e-11	0.014
cyclohexane	6.97e-12	0.014
cyclohexanone	6.4e-12	0.051
cyclopentane	4.97e-12	0.005
ethane	2.48e-13	0.264
ethyl alcohol	3.58e-12	0.005
ethylbenzene	7e-12	0.144
ethylene	8.52e-12	6.670
formaldehyde	9.37e-12	6.823
indan	1.9e-11	0.088
isobutane	2.44e-12	0.566
isobutylene	5.14e-11	0.427
butylbenzene	4.5e-12	0.060
diethylbenzene	8.11e-12	0.065
isopentane	3.6e-12	0.278
isopropylbenzene	6.9e-12	0.009
m-xylene	2.31e-11	0.283
methane	6.4e-15	1.892
methyl alcohol	6.16e-13	0.014
methyl ethyl ketone	1.22e-12	0.686
2-hexanone	9.1e-12	0.417
methylcyclohexane	9.64e-12	0.032
methylcyclopentane	5.66e-12	0.070
n-butane	2.36e-12	0.046
n-decane	1.1e-11	0.246
n-heptane	6.76e-12	0.032
n-hexane	5.2e-12	0.074
n-nonane	9.7e-12	0.107
n-octane	8.11e-12	0.065
n-pentane	3.8e-12	0.083
n-propylbenzene	5.8e-12	0.056
n-undecane	1.23e-11	0.121
naphthalene	2.3e-11	0.042
o-xylene	1.36e-11	0.158
p-xylene	1.43e-11	0.046
propane	1.09e-12	0.088
propionaldehyde	2.2e-11	0.450

propylene	2.64e-11	1.206
styrene	5.8e-11	0.028
t-butylbenzene	4.5e-12	0.005
unknown	1.23e-11	0.093
trans-2-butene	6.4e-11	0.019
trans-2-pentene	6.7e-11	0.682
toluene	5.63e-12	2.268
C_{12} branched alkane	1.82E-11	1.623
C_{13} branched alkane	1.68E-11	1.052
C_{14} branched alkane	1.39E-11	0.939
C_{15} branched alkane	1.82E-11	0.988
C_{16} branched alkane	1.96E-11	0.440
C_{17} branched alkane	2.1E-11	0.573
C_{18} branched alkane	2.24E-11	0.343
C_{19} branched alkane	2.38E-11	0.194
C_{20} branched alkane	2.52E-11	0.128
C_{21} branched alkane	2.67E-11	0.121
C_{22} branched alkane	2.81E-11	8.690
C_{12} cyclic alkane	1.82E-11	8.858
C_{13} cyclic alkane	1.68E-11	6.299
C_{14} cyclic alkane	1.39E-11	5.723
C_{15} cyclic alkane	1.82E-11	4.372
C_{16} cyclic alkane	1.96E-11	3.711
C_{17} cyclic alkane	2.1E-11	3.382
C_{18} cyclic alkane	2.24E-11	2.115
C_{19} cyclic alkane	2.38E-11	1.181
C_{20} cyclic alkane	2.52E-11	0.748
C_{21} cyclic alkane	2.67E-11	0.629
C_{22} cyclic alkane	2.81E-11	1.167
n-dodecane	1.82E-11	1.094
tridecane	1.68E-11	0.730
tetradecane	1.39E-11	0.613
pentadecane	1.82E-11	0.456
hexadecane	1.96E-11	0.331
heptadecane	2.1E-11	0.296
octadecane	2.24E-11	0.145
nonadecane	2.38E-11	0.073
eicosane	2.52E-11	0.044
heneicosane	2.67E-11	0.029
docosane	2.81E-11	0.287
pristane	2.44E-11	0.160
phytane	2.61E-11	0.208
naphthalene	1.3E-11	0.023
phenanthrene	1.30E-11	0.023

Table 12:VOC emissions profile #4777- Biodiesel Exhaust-Light Duty Truck; Cold Start

Species Name	***kOH (cm^3 $molecules^{-1}s^{-1}$)***	***Mass Percent***
1,1,4-trimethylcyclohexane	9.09E-12	0.081
1,2,4-trimethylbenzene	1.67E-11	0.405
1,2-dimethyl-4-ethylbenzene	1.69E-11	0.177
1,3,5-trimethylbenzene	3.51E-11	0.162
1,3-dimethyl-2-ethylbenzene	1.76E-11	0.283
1,4-dimethyl-2-ethylbenzene	1.69E-11	0.374
1-(1,1-dimethylethyl)-3,5-dimethylbenzene	3.01E-11	0.319
1-butene	3.14E-11	0.521
1-ethyl-1-methylcyclopentane	6.33E-12	0.035
1-hexene	3.02E-11	0.152
1-methyl-2-ethylbenzene	7.44E-12	0.329
1-methyl-2-tert-butylbenzene	6.74E-12	0.369
1-methyl-3-ethylbenzene	1.39E-11	0.617
1-methyl-3-isopropylbenzene	1.45E-11	0.379
1-methyl-3-propylbenzene	1.52E-11	0.233
1-methyl-4-ethylbenzene	7.44E-12	0.182
1-nonene	3.44E-11	0.061
1-pentene	3.14E-11	0.273
1-tert-butyl-4-ethylbenzene	7.42E-12	0.167
2,2,4-trimethylpentane	3.16E-11	0.197
2,2-dimethylbutane	1.82E-12	0.101
2,2-dimethylpropane	6.69E-13	0.051
2,3,4-trimethylpentane	8.54E-12	0.046
2,3-dimethylbutane	5.44E-12	0.020
2,3-dimethylhexane	5.09E-12	0.106
2,3-dimethylpentane	7.14E-12	0.015
2,4-dimethylhexane	4.92E-12	0.051
2,4-dimethylpentane	6.85E-12	0.010
2,5-dimethylheptane	9.97E-12	0.071
2,5-dimethylhexane	7.24E-12	0.025
2-methyl-butyl-benzene	1.02E-11	0.946
2-methylhexane	6.86E-12	0.293
2-methylnonane	1.11E-11	0.273
2-methyloctane	9.97E-12	0.091
2-methylpentane	5.45E-12	0.040

3,3-dimethyloctane	7.21E-12	0.263
3,3-dimethylpentane	2.97E-12	0.081
3,5-dimethylheptane	1.02E-11	0.076
3-ethyloctane	1.18E-11	0.162
3-ethylpentane	7.56E-12	0.030
3-methyl-1-butene	2.86E-11	0.111
3-methyl-cis-2-pentene	8.83E-11	0.071
3-methylheptane	8.56E-12	0.056
3-methylhexane	7.15E-12	0.020
3-methylnonane	1.14E-11	0.228
3-methylpentane	5.73E-12	0.071
4-methyl-1-pentene	3.02E-11	0.061
4-methylheptane	1.02E-11	0.475
acetaldehyde	1.5E-11	2.710
acetone	1.7E-13	3.828
acetylene	8.15E-13	2.346
acrolein	2.58E-11	0.759
benzene	1.22E-12	1.370
cis,trans-1,2,4-trimethylcyclohexane	1.35E-11	3.580
cis-2-butene	5.64E-11	0.056
cis-2-nonene	6.32E-11	0.096
cis-2-octene	6.18E-11	0.046
cis-3-hexene	2E-10	0.066
crotonaldehyde	3.62E-11	0.228
cyclohexane	6.97E-12	0.015
cyclohexane	6.97E-12	0.071
cyclopentane	4.97E-12	0.030
cyclopentene	5.88E-11	0.046
ethane	2.48E-13	0.172
ethylbenzene	7E-12	0.071
ethylene	8.52E-12	10.013
formaldehyde	9.37E-12	9.330
isobutane	2.44E-12	0.030
isopentane	3.6E-12	0.344
isopropylcyclohexane	1.34E-11	0.126
isopropyltoluene	8.54E-12	0.308
m & *p*-xylene	2.31E-11	0.319
2-butanone	1.22E-12	1.643
methylbutadiene	1.05E-10	0.091
methylcyclohexane	5.09E-12	0.086
methylcyclopentane	5.66E-12	0.030
n-butane	2.36E-12	0.081
n-butylcyclopentane	1.01E-11	0.137
n-decane	1.1E-11	1.461

n-dodecane	1.39E-11	1.193
n-heptane	6.76E-12	0.040
n-hexane	5.2E-12	0.152
n-nonane	9.7E-12	0.738
n-octane	8.11E-12	0.415
n-pentane	3.8E-12	0.076
n-pentylbenzene	1.01E-11	0.182
n-propylbenzene	5.8E-12	0.137
n-tridecane	1.53E-11	0.526
n-undecane	1.23E-11	1.664
o-xylene	1.36E-11	0.339
propane	1.09E-12	0.025
propionaldehyde	2.2E-11	0.541
propylcyclopentane	1.2E-11	0.051
propylene	2.64E-11	2.195
toluene	5.63E-12	1.406
trans-1,2-dimethylcyclopentane	6.8E-12	1.310
trans-1,4-dimethylcyclohexane	1.19E-11	0.056
trans-2-butene	6.4E-11	0.076
trans-2-heptene	6.8E-11	0.030
trans-2-octene	6.94E-11	0.071
trans-2-pentene	6.7E-11	0.046
trans-3-nonene	7.04E-11	0.000
C_{12} branched alkane	1.82E-11	1.623
C_{13} branched alkane	1.68E-11	1.052
C_{14} branched alkane	1.39E-11	0.939
C_{15} branched alkane	1.82E-11	0.988
C_{16} branched alkane	1.96E-11	0.440
C_{17} branched alkane	2.1E-11	0.573
C_{18} branched alkane	2.24E-11	0.343
C_{19} branched alkane	2.38E-11	0.194
C_{20} branched alkane	2.52E-11	0.128
C_{21} branched alkane	2.67E-11	0.121
C_{22} branched alkane	2.81E-11	8.690
C_{12} cyclic alkane	1.82E-11	8.858
C_{13} cyclic alkane	1.68E-11	6.299
C_{14} cyclic alkane	1.39E-11	5.723
C_{15} cyclic alkane	1.82E-11	4.372
C_{16} cyclic alkane	1.96E-11	3.711
C_{17} cyclic alkane	2.1E-11	3.382
C_{18} cyclic alkane	2.24E-11	2.115
C_{19} cyclic alkane	2.38E-11	1.181
C_{20} cyclic alkane	2.52E-11	0.748

C_{21} cyclic alkane	2.67E-11	0.629
C_{22} cyclic alkane	2.81E-11	1.167
n-dodecane	1.82E-11	1.094
tridecane	1.68E-11	0.730
tetradecane	1.39E-11	0.613
pentadecane	1.82E-11	0.456
hexadecane	1.96E-11	0.331
heptadecane	2.1E-11	0.296
octadecane	2.24E-11	0.145
nonadecane	2.38E-11	0.073
eicosane	2.52E-11	0.044
heneicosane	2.67E-11	0.029
docosane	2.81E-11	0.287
pristane	2.44E-11	0.160
phytane	2.61E-11	0.208
naphthalene	1.3E-11	0.023
phenanthrene	1.30E-11	0.023

Table 13:EPA #4771 Biodiesel Exhaust-Light Duty Truck; Cold Start

Species Name	***kOH (cm^3 $molecules^{-1}s^{-1}$)***	***Mass Percent***
1,1,2-trimethylcyclohexane	9.09E-12	0.043
1,2,3-trimethylbenzene	1.67E-11	0.495
1,2,4-trimethylbenzene	1.67E-11	0.319
1,2-dimethyl-4-ethylbenzene	1.69E-11	0.229
1,3,5-trimethylbenzene	3.51E-11	0.125
1,4-dimethyl-2-ethylbenzene	1.69E-11	0.312
1-(1,1-dimethylethyl)-3,5-dimethylbenzene	3.01E-11	0.262
1-butene	3.14E-11	0.269
1-hexene	3.02E-11	0.072
1-methyl-2-ethylbenzene	7.44E-12	0.272
1-methyl-2-tert-butylbenzene	6.74E-12	0.244
1-methyl-3-ethylbenzene	1.39E-11	0.244
1-methyl-3-propylbenzene	1.52E-11	0.215
1-methyl-4-ethylbenzene	7.44E-12	0.036
1-nonene	3.44E-11	0.032
1-octene	3.30E-11	0.032
1-pentene	2.88E-11	0.147
1-tert-butyl-4-ethylbenzene	7.42E-12	0.161
2,2-dimethylbutane	1.82E-12	0.032
2,2-dimethylpropanal	2.24E-11	0.344
2,3-dimethylhexane	2.24E-11	0.061
2,5-dimethylheptane	9.97E-12	0.054

2-methyl-2-butene	8.73E-11	0.025
2-methyl-butyl-benzene	1.02E-11	0.380
2-methylhexane	6.86E-12	0.047
2-methylnonane	1.11E-11	0.133
2-methyloctane	9.97E-12	0.079
3,3-dimethylheptane	1.02E-11	0.054
3,3-dimethyloctane	7.21E-12	0.165
3-ethylpentane	7.56E-12	0.025
3-methyl-1-butene	2.86E-11	0.043
3-methylhexane	7.15E-12	0.004
3-methylnonane	1.14E-11	0.412
3-methylpentane	5.73E-12	0.022
4-methyl-1-pentene	3.02E-11	0.047
4-methylheptane	1.02E-11	0.272
acetaldehyde	1.5E-11	2.320
acetone	1.7E-13	2.015
acetylene	8.15E-13	1.334
acrolein	2.58E-11	0.907
benzaldehyde	1.2E-11	0.190
benzene	1.22E-12	0.767
1,2,4-trimethylcyclohexane	1.35E-11	2.309
cis-2-nonene	6.32E-11	0.065
cis-3-hexene	2E-10	0.043
crotonaldehyde	3.62E-11	0.272
cyclohexane	6.97E-12	0.011
cyclohexane	6.97E-12	0.068
cyclopentane	4.97E-12	0.022
cyclopentene	5.88E-11	0.018
ethylbenzene	7E-12	0.337
ethylene	8.52E-12	5.532
formaldehyde	9.37E-12	7.594
isobutane	2.44E-12	0.004
isopropylcyclohexane	1.34E-11	0.068
isopropyltoluene	8.54E-12	0.208
m & p-xylene	2.31E-11	0.229
2-butanone	1.22E-12	0.660
methylbutadiene	1.05E-10	0.068
methylcyclohexane	5.09E-12	0.050
methylcyclopentane	5.66E-12	0.018
n-butylcyclopentane	1.01E-11	0.061
n-decane	1.1E-11	0.861
n-dodecane	1.39E-11	0.674
n-heptane	6.76E-12	0.100
n-hexane	5.2E-12	0.068
n-nonane	9.7E-12	0.477

n-octane	8.11E-12	0.197
n-pentane	3.8E-12	0.011
n-propylbenzene	5.8E-12	0.022
n-tridecane	1.53E-11	0.491
n-undecane	1.23E-11	1.223
o-xylene	1.36E-11	0.179
propane	1.09E-12	0.011
propionaldehyde	2.2E-11	0.409
propylcyclopentane	1.2E-11	0.032
propylene	2.64E-11	2.273
toluene	5.63E-12	0.925
trans-1,2-dimethylcyclopentane	6.8E-12	0.717
trans-1,4-dimethylcyclohexane	1.19E-11	0.039
trans-2-octene	6.94E-11	0.039
trans-2-pentene	6.7E-11	0.029
trans-3-nonene	7.04E-11	0.039
valeraldehyde	2.74E-11	0.305
C_{12} branched alkane	1.82E-11	1.623
C_{13} branched alkane	1.68E-11	1.052
C_{14} branched alkane	1.39E-11	0.939
C_{15} branched alkane	1.82E-11	0.988
C_{16} branched alkane	1.96E-11	0.440
C_{17} branched alkane	2.1E-11	0.573
C_{18} branched alkane	2.24E-11	0.343
C_{19} branched alkane	2.38E-11	0.194
C_{20} branched alkane	2.52E-11	0.128
C_{21} branched alkane	2.67E-11	0.121
C_{22} branched alkane	2.81E-11	8.690
C_{12} cyclic alkane	1.82E-11	8.858
C_{13} cyclic alkane	1.68E-11	6.299
C_{14} cyclic alkane	1.39E-11	5.723
C_{15} cyclic alkane	1.82E-11	4.372
C_{16} cyclic alkane	1.96E-11	3.711
C_{17} cyclic alkane	2.1E-11	3.382
C_{18} cyclic alkane	2.24E-11	2.115
C_{19} cyclic alkane	2.38E-11	1.181
C_{20} cyclic alkane	2.52E-11	0.748
C_{21} cyclic alkane	2.67E-11	0.629
C_{22} cyclic alkane	2.81E-11	1.167
n-dodecane	1.82E-11	1.094
tridecane	1.68E-11	0.730
tetradecane	1.39E-11	0.613
pentadecane	1.82E-11	0.456
hexadecane	1.96E-11	0.331
heptadecane	2.1E-11	0.296

octadecane	2.24E-11	0.145
nonadecane	2.38E-11	0.073
eicosane	2.52E-11	0.044
heneicosane	2.67E-11	0.029
docosane	2.81E-11	0.287
pristane	2.44E-11	0.160
phytane	2.61E-11	0.208

Table 14:VOC emissions profile #8774- Diesel Exhaust Emissions from Pre-2007 Model Year Heavy-Duty Diesel Trucks

Species Name	***kOH (cm^3 $molecules^{-1}$ s^{-1})***	***Mass Percent***
1,2,3,5-tetramethylbenzene	4.30705E-10	0.069
1,2,3-trimethylbenzene	3.27E-10	0.050
1,2,4,5-tetramethylbenzene	2.05132E-10	0.033
1,2,4-trimethylbenzene	3.25E-10	0.021
1,2-butadiene	6.66E-10	0.010
1,3,5-trimethylbenzene	5.67E-10	0.042
1,3-butadiene	6.66E-10	0.344
1,3-diethylbenzene	1.42418E-10	0.068
1,3-hexadiene	1.06101E-09	0.015
1,4-diethylbenzene	8.1054E-11	0.091
1-butene	3.14E-10	0.872
1-heptene	3.159E-10	0.152
1-methyl-2-ethylbenzene	7.4388E-11	0.078
1-methyl-3-ethylbenzene	1.388E-10	0.047
1-methyl-4-ethylbenzene	7.4388E-11	0.039
1-methylindan	9.1645E-11	0.028
1-pentene	3.14E-10	0.183
1-propyne	7.136E-11	0.089
2,2,4-trimethylpentane	3.34E-11	0.262
2,2,5-trimethylhexane	6.0487E-11	0.057
2,2-dimethylbutane	1.8179E-11	0.043
2,3,4-trimethylpentane	6.6E-11	0.032
2,3-dimethyl-2-pentene	1.11509E-09	0.002
2,3-dimethylbutane	5.4415E-11	0.067
2,3-dimethylhexane	8.5522E-11	0.007
2,3-dimethylpentane	7.13E-11	0.078
2,4-dimethylpentane	4.77E-11	0.243
2,6-dimethylheptane	9.6807E-11	0.000
2-methyl-1-butene	5.26373E-10	0.103
2-methyl-1-pentene	5.40009E-10	2.833
2-methyl-2-butene	8.7308E-10	0.117

2-methyl-2-pentene	8.82733E-10	0.012
2-methylheptane	8.276E-11	0.062
2-methylhexane	6.863E-11	0.070
2-methylindan	9.419E-11	0.017
2-methylpentane	5.2E-11	0.039
3-methyl-cis-2-pentene	8.8273E-10	0.009
3-methyl-trans-2-pentene	8.82733E-10	0.111
3-methylheptane	8.5606E-11	0.054
3-methylhexane	7.1476E-11	0.130
3-methyloctane	9.9737E-11	0.142
4-methylheptane	8.276E-11	0.018
acetaldehyde	1.5E-10	2.228
acetylene	8.15E-12	2.675
alpha-pinene	9.07477E-10	0.035
benzaldehyde	1.2E-10	0.231
benzene	1.22E-11	1.281
beta-pinene	5.65247E-10	0.001
butyraldehyde	2.4E-10	0.514
cis-2-butene	5.64E-10	0.098
cis-2-hexene	5.90009E-10	0.021
cis-2-pentene	6.5E-10	0.053
crotonaldehyde	3.619E-10	0.128
cyclohexane	6.97E-11	0.120
cyclohexene	6.15237E-10	0.051
cyclopentane	4.97E-11	0.038
cyclopentene	5.87748E-10	0.060
dl-limonene	1.45218E-09	0.012
ethane	2.48E-12	0.739
ethylbenzene	7E-11	0.147
ethylene	8.52E-11	8.180
formaldehyde	9.37E-11	3.554
glyoxal	2.5317E-10	0.296
indan	8.2777E-11	0.028
isobutane	2.4418E-11	0.305
isopentane	3.6E-11	1.721
isoprene	1.05E-09	0.061
isopropylbenzene	6.9E-11	0.013
isopropylcyclohexane	1.33E-10	0.150
isopropyltoluene	8.536E-11	0.062
m & *p*-xylene	2.31E-10	0.252
2-butanone	1.22E-11	1.198
methylcyclohexane	9.64E-11	0.115
methylcyclopentane	5.66E-11	1.786
n-butane	2.36E-11	0.573
n-butylbenzene	8.723E-11	0.021

n-decane	1.1E-10	0.404
n-heptane	6.76E-11	0.125
n-hexane	5.2E-11	0.307
n-nonane	9.7E-11	0.159
n-octane	8.11E-11	0.145
n-pentane	3.8E-11	0.313
n-propylbenzene	5.8E-11	0.026
n-undecane	1.23E-10	0.417
o-xylene	1.36E-10	0.104
propane	1.09E-11	0.890
propionaldehyde	2.19E-10	0.257
propylene	2.64E-10	2.347
propyltoluene	8.80E-11	0.050
styrene	5.8E-10	0.129
tolualdehyde	1.86E-10	0.016
toluene	5.63E-11	0.588
trans-1,3-dichloropropene	9.35E-11	0.002
trans-2-butene	6.4E-10	0.121
trans-2-hexene	6.66E-10	0.036
trans-2-pentene	6.7E-10	0.054
unknown	2.7E-10	0.000
valeraldehyde	2.74E-10	0.023
C_{12} branched alkane	1.82E-11	1.623
C_{13} branched alkane	1.68E-11	1.052
C_{14} branched alkane	1.39E-11	0.939
C_{15} branched alkane	1.82E-11	0.988
C_{16} branched alkane	1.96E-11	0.440
C_{17} branched alkane	2.1E-11	0.573
C_{18} branched alkane	2.24E-11	0.343
C_{19} branched alkane	2.38E-11	0.194
C_{20} branched alkane	2.52E-11	0.128
C_{21} branched alkane	2.67E-11	0.121
C_{22} branched alkane	2.81E-11	8.690
C_{12} cyclic alkane	1.82E-11	8.858
C_{13} cyclic alkane	1.68E-11	6.299
C_{14} cyclic alkane	1.39E-11	5.723
C_{15} cyclic alkane	1.82E-11	4.372
C_{16} cyclic alkane	1.96E-11	3.711
C_{17} cyclic alkane	2.1E-11	3.382
C_{18} cyclic alkane	2.24E-11	2.115
C_{19} cyclic alkane	2.38E-11	1.181
C_{20} cyclic alkane	2.52E-11	0.748
C_{21} cyclic alkane	2.67E-11	0.629
C_{22} cyclic alkane	2.81E-11	1.167
n-dodecane	1.82E-11	1.094

tridecane	1.68E-11	0.730
tetradecane	1.39E-11	0.613
pentadecane	1.82E-11	0.456
hexadecane	1.96E-11	0.331
heptadecane	2.1E-11	0.296
octadecane	2.24E-11	0.145
nonadecane	2.38E-11	0.073
eicosane	2.52E-11	0.044
heneicosane	2.67E-11	0.029
docosane	2.81E-11	0.287
pristane	2.44E-11	0.160
phytane	2.61E-11	0.208
naphthalene	1.3E-11	0.023
phenanthrene	1.30E-11	0.023

Table 15:SOM parameters from Cappa et al. (2016) to simulate SOA formation assuming a low estimate for vapor wall loss rates ($1x10^{-4}$ s^{-1}).

Species	m_{frag}	***ΔLVP***	$p_{O,1}$	$p_{O,2}$	$p_{O,3}$	$p_{O,4}$	***Primary Reference***
n-dodecane	0.186	1.45	0.961	0.001	0.002	0.036	Loza et al. (2014)
methylundecane	0.0937	1.07	0.257	0.001	0.741	0.002	Loza et al. (2014)
hexylcyclohexane	0.155	1.86	0.907	0.001	0.091	0.001	Loza et al. (2014)
toluene	5	1.37	0.865	0.001	0.065	0.069	Zhang et al. (2014)
benzene	0.73	1.47	0.017	0.001	0.981	0.001	Ng et al. (2007)
m-xylene	0.0389	1.46	0.001	0.001	0.905	0.093	Ng et al. (2007)
naphthalene	0.643	1.41	0.835	0.001	0.001	0.162	Chan et al. (2009)

Table 16:SOM parameters from Cappa et al. (2016) to simulate SOA formation assuming a high estimate for vapor wall loss rates ($2.5x10^{-4}$ s^{-1}).

Species	m_{frag}	***ΔLVP***	$p_{O,1}$	$p_{O,2}$	$p_{O,3}$	$p_{O,4}$	***Primary Reference***
n-dodecane	0.266	1.47	0.965	0.001	0.002	0.032	Loza et al. (2014)
methylundecane	0.254	0.94	0.377	0.001	0.622	0.001	Loza et al. (2014)
hexylcyclohexane	0.274	1.82	0.942	0.001	0.002	0.055	Loza et al. (2014)
toluene	4.61	1.42	0.856	0.001	0.002	0.141	Zhang et al. (2014)
benzene	0.824	1.53	0.008	0.001	0.991	0.001	Ng et al. (2007)
m-xylene	0.101	1.21	0.001	0.001	0.315	0.683	Ng et al. (2007)
naphthalene	1.69	1.53	0.878	0.001	0.002	0.119	Chan et al. (2009)